A high-content siRNA screen reveals new regulators of nuclear membrane stability

Amanda L. Gunn, Artem I. Yashchenko, Emily M. Hatch*

Divisions of Basic Sciences and Human Biology, The Fred Hutchinson Cancer Center, 1100 Fairview Ave, Seattle, Washington 98109, USA.

Running head: CTDNEP1 regulates nuclear membrane stability

*Corresponding author
Emily M. Hatch
Phone: (206) 667-5116
E-mail: ehatch@fredhutch.org

Character count:

Abbreviations:
53BP1: p53 binding protein 1
BAF: Barrier to Autointegration factor
cGAS: cyclic GMP-AMP synthase
CTDNEP1: CTD nuclear envelope phosphatase 1
GO: Gene Ontology
HSP90: Heat shock protein 90
INM: Inner nuclear membrane
NES: Nuclear export signal
NLS: Nuclear localization signal
ONM: Outer nuclear membrane
PML bodies: Promyelocytic leukemia bodies

Abstract

Nuclear membrane rupture is a physiological response to *in vivo* situations, such as cell migration. When disregulated, it can have deleterious consequences for the cell including increased genome instability and inflammatory signaling. However, many of the molecular mechanisms underlying this process are unclear and only a few regulators have been uncovered. In this study, we developed a nuclear rupture reporter that is size-excluded from re-compartmentalization following nuclear rupture events. This allows for robust detection of factors influencing nuclear integrity in fixed cells. Additionally, we created and validated an automated pipeline for the analysis of fixed cell images that we applied in a high-content siRNA screen. Our screen identified conditions that led to both increased and decreased nuclear rupture frequency. Analysis of the hits demonstrated an enrichment in factors in the nuclear membrane and ER, and demonstrated that nuclear size is not strongly correlated with rupture frequency. Based on these results, we validated a new function for the protein phosphatase CTDNEP1 in maintaining nucleus stability. These findings provide new insights into the regulation of nuclear stability and define a novel method of rupture analysis that removes a substantial barrier to understanding the molecular mechanisms underlying this process.

Introduction

The nucleus is separated from the cytosol by the inner and outer membranes (INM and ONM), which are contiguous with the ER and joined at nuclear pore complexes. In the nucleus, interactions between proteins in the INM and ONM, the underlying nuclear lamina, and peripherally localized heterochromatin provide essential support for the nucleus and regulate mechanical signaling (Niethammer, 2021; Maurer and Lammerding, 2019). These interactions undergo extensive remodeling to enable various nuclear membrane dynamics, including nuclear envelope breakdown and assembly, membrane fusion, budding, and interphase rupture and repair. These dynamics have been identified in organisms ranging from yeast to humans and are critical for cell functioning and development (King and Lusk, 2016). Changes in nuclear membrane stability underlie pathogen infection, neurodegeneration, autoimmune diseases, cancer progression, and laminopathy pathologies (Maciejowski and Hatch, 2020; Ungricht and Kutay, 2017), suggesting that nuclear envelope structure must be strictly regulated for proper cell functioning.

Nuclear membrane rupture is defined as the rapid loss of nucleus compartmentalization in interphase resulting in the mixing of nuclear and cytoplasmic proteins and organelles (Vos et al., 2011; Noronha et al., 2001; Vargas et al., 2012). In the nucleus, membrane rupture is typically repaired within minutes with limited effects on cell proliferation or viability (Raab et al., 2016; Denais et al., 2016). However, it can cause DNA damage, and activation of cell invasion and inflammation pathways, especially in conjunction with mechanical stress (Nader et al., 2021a; Raab et al., 2016; Denais et al., 2016; Shah et al., 2020; Irianto et al., 2017; Earle et al., 2020). These pathways are even more highly activated by rupture of micronuclei, small nuclear compartments that form around missegregated chromatin in metazoans, which frequently fail to repair their membrane leaving chromatin in the cytoplasm for the duration of interphase (Guscott et al., 2022; Krupina et al., 2021). Nuclear membrane rupture has been identified in a range of mechanically challenging conditions *in vivo,* including migration through dense extracellular matrices, at the leading edge of tumors, and during nuclear migration in fission yeast, *C. elegans*, and mouse models of laminopathies (Earle et al., 2020; Nader et al., 2021a; Silva et al., 2022; Raab et al., 2016; Penfield et al., 2018; Denais et al., 2016; Kinugasa et al., 2019; Hirano et al., 2020; Chen et al., 2019; Kim et al., 2021), indicating that nuclear membrane rupture is a physiological response to a wide-range of *in vivo* conditions.

A current model of nuclear membrane rupture is that it occurs in response to an imbalance between force and force resistance at the nuclear envelope, which causes the membranes to stretch and eventually rupture (Nader et al., 2021b; Zhang et al., 2019; Xia et al., 2018). However, the molecular underpinnings of both rupture and repair are largely unknown. Changes in nuclear membrane morphology generally require local or global loss of membrane attachment to the nuclear lamina, with membrane rupture typically occurring at lamina gaps that lack lamin proteins, INM proteins, and nuclear pores (Maciejowski and Hatch, 2020). As force is applied to the nucleus, the membrane at this gap blebs out, sometimes accompanied by euchromatin (Shimi et al., 2008; Pfleghaar et al., 2015; Stephens et al., 2017). Increasing the amount of heterochromatin or lamina proteins is proposed to prevent rupture by increasing mechanical resistance and limiting lamina gaps and membrane blebs (Stephens et al., 2017; Vargas et al., 2012; Hatch et al., 2013; Maciejowski et al., 2015; Robijns et al., 2016; Xia et al., 2019; Chen et al., 2021). At some point the bleb stops expanding and both

membranes rupture (Chen et al., 2018), leading to diffusion of soluble proteins and small organelles through the rupture down their concentration gradient (Houben et al., 2013; Vos et al., 2011; Vargas et al., 2012; Zhang et al., 2019). Chromatin-directed membrane repair initiates within seconds of the chromatin being exposed to the cytoplasm through the actions of BAF, interacting transmembrane proteins, and the ESCRT-III membrane remodeling complex (Halfmann et al., 2019; Young et al., 2020; Vietri et al., 2020; Denais et al., 2016). After repair, proteins containing nucleus sorting signals are recompartmentalized, but proteins and organelles lacking nuclear sorting signals (NLS and NES) can persist in the wrong compartment for several hours (Irianto et al., 2017; Earle et al., 2020; Houben et al., 2013). Many questions about this process remain, including how lamina gaps form, what triggers the transition from membrane expansion to membrane rupture, and how the frequency and size of the ruptures affects the cellular consequences of losing nucleus compartmentalization.

The gold standard for identifying and quantifying nuclear membrane rupture is live cell imaging of a fluorescent protein tagged with a nuclear localization signal (NLS). Although software exists to automatically quantify ruptures from this type of data (Robijns et al., 2016), the sheer amount of data and imaging time required precludes systematic identification of membrane stability regulators using this method. The search for a fixed-cell reporter for nuclear membrane rupture has identified several proteins that localize to rupture sites and persist as foci for some time after membrane repair, including cGAS, BAF, and lamin A (Denais et al., 2016; Raab et al., 2016). However, the extent and duration of their localization can be highly variable and dependent on additional factors (Guey et al., 2020; MacDonald et al., 2023). Alternatively, mislocalization of large proteins that fail to recompartmentalize after repair, including Hsp90, 53BP1, and PML bodies, can be used to identify previously ruptured nuclei (Earle et al., 2020; Irianto et al., 2017; Xia et al., 2018; Houben et al., 2013; Cho et al., 2019). Building on these observations, we developed a reliable and well-tolerated reporter of nuclear membrane rupture that can be used in fixed cells that we call RFP-Cyto. We demonstrate that mislocalization of RFP-Cyto to the nucleus is a rapid, precise, and durable marker of nuclear membrane rupture. We describe a fully automated imaging pipeline to quantify rupture frequency in fixed cell populations using this reporter and combine it with siRNA screening to discover new regulators of rupture in a high-throughput and unbiased manner. In our initial analysis we identify 22 factors not previously known to regulate nucleus stability that either stabilize or destabilize the nuclear membrane upon depletion. These results provide new insights into the mechanism by which nuclear stability is regulated and define a new method of analysis that removes a substantial barrier to defining the molecular mechanisms of this process.

Results

A fixed-cell reporter for nuclear membrane rupture

To develop a fixed cell reporter for interphase nuclear rupture, we took advantage of the fact that large objects and proteins lacking a nuclear/cytoplasm sorting signal remain mislocalized after nuclear membrane rupture and repair. We identified a construct containing luciferase tagged with two RFPs as the smallest one (118 kD, RFP-Cyto) that showed exclusive cytoplasm localization during interphase (data not shown). We optimized for a minimally sized reporter to increase the likelihood that small, short ruptures would result in reporter mislocalization (Fig. 1A). In contrast to fluorescent proteins tagged with an NLS (GFP-Nuc), we

expected that RFP-Cyto would remain mislocalized in the nucleus after membrane repair (Fig. 1A-B). To test this hypothesis, we stably co-expressed RFP-Cyto in U2OS cells expressing GFP-Nuc and an shRNA against LMNB1 and monitored RFP-Cyto localization during nuclear rupture by live-cell imaging. Constitutive expression of anti-LMNB1 shRNAs in U2OS cells leads to a modest reduction in protein levels, which, coupled with actin-dependent nuclear compression during S phase arrest, substantially increases nuclear rupture frequency and allows identification of *in vivo* relevant mechanisms (Hatch and Hetzer, 2016; Young et al., 2020; Aureille et al., 2019). This cell line, called U2OS RuptR, was imaged for 20 h with a pass time of 3 m, and subsequently analyzed for GFP and RFP mean nuclear intensities during rupture events. We found that RFP-Cyto intensity increased in the nucleus after rupture, indicated by a decrease in GFP-Nuc signal, and remained mislocalized after membrane repair, indicated by GFP-Nuc recompartmentalization. In the absence of nuclear rupture, no change in RFP-Cyto nuclear intensity was observed (Fig. 1C-D, Fig. S1B, Movie S1). RFP-Cyto localization to the nucleus accurately predicted nuclear rupture events, with an average precision of 99% and an average recall of 99% (Fig. 1E). Ruptures that were missed by the reporter tended to be in cells that had a combination of low cytoplasmic RFP-Cyto intensity and a very short rupture. As expected, RFP-Cyto was excluded from post-mitotic nuclei soon after nuclear envelope assembly finished (time of max GFP-Nuc intensity) (Fig. S1C, Movie S2)(Cuylen-Haering et al., 2020; Samwer et al., 2017). Apparent delays in exclusion are likely due to out-of-focus RFP-Cyto signal from the cytoplasm as the chromatin decondenses, as complete segregation coincides with the end of GFP-Nuc signal expansion.

To determine whether RFP-Cyto localization was sufficiently sensitive to detect biologically relevant changes in nuclear rupture frequency, we depleted lamin B1, lamin A/C, or Sun1 using single siRNAs in U2OS RuptR cells and compared nuclear rupture frequencies after quantification by live-cell imaging or fixed cell analysis. Transfection of siRNAs against LMNB1 in this cell line induces substantially more protein loss (Hatch et al., 2013). As expected, lamin B1 loss increased rupture frequency and depletion of Sun1 suppressed nuclear membrane rupture in our live-cell imaging analysis of GFP-Nuc localization (Hatch and Hetzer, 2016; Hatch et al., 2013). We initially expected lamin A/C depletion to increase rupture frequency (Robijns et al., 2016; Vos et al., 2011), but, in line with recent results from other systems, we did not see a consistent effect of lamin A/C loss on rupture frequency (Pho et al., 2022; Chen et al., 2018). Similar results were observed when ruptures were analyzed by fixed-cell analysis of RFP-Cyto localization (Fig. 1F, S1A), demonstrating that this method provides accurate information about relative rupture frequency that can be used to identify new determinants of nuclear stability.

<u>RNAi screen for regulators of nuclear membrane rupture (high statistical power)</u>

To enable high throughput analysis of RFP-Cyto localization and intensity, we developed a segmentation strategy in CellProfiler (Carpenter et al., 2006) coupled with a set of post-segmentation intensity and morphological filters to remove several classes of contaminating objects. The processing pipeline was developed on U2OS RuptR cells transfected with a control siRNA, arrested in S phase for 24 h, fixed, and labeled with Hoechst to mimic screening conditions (Fig. 2A). Nuclei and cells were segmented in CellProfiler based on Hoechst and RFP-Cyto signal, respectively, using standard modules, and morphological parameters

were analyzed (Fig. S2A, Fig. 2C). Objects were then shrunk to limit overlapping signal and segmentation errors and RFP and Hoechst mean intensity in the cytoplasm (RFP) and nucleus (RFP and Hoechst) were measured. Intensity and morphology filters were applied post-processing to eliminate data from cells with low RFP-Cyto expression, missegmented objects, mitotic or dead cells, and out of focus cells. Mitotic cells were eliminated by setting a maximum Hoechst intensity threshold, coupled with a maximum solidity threshold, and out of focus cells were reduced by setting a minimum Hoechst intensity threshold. Cells undergoing cell death were removed by setting minimum nuclear size and solidity thresholds. Filter thresholds were set globally for intensity measurements and per condition for morphology measurements to accommodate expected variations in nucleus shape and size during screening (Fig. 2B-D, Fig. S2A). After filtering, approximately 75% of cells were retained and analyzed for RFP-Cyto localization by calculating the nuclear to cytoplasm (nuc:cyto) mean intensity ratio (Fig. 2D).

We applied this image analysis pipeline to identify new regulators of nuclear membrane rupture in an siRNA screen. U2OS RuptR cells were reverse transfected in 96-well plates with pools of four siRNAs targeting genes from known categories of nuclear membrane stability regulators in mammalian cells (49%) and randomly selected genes (51%). Targeted categories included chromatin organization (Stephens et al., 2017), tumor suppressors (Yang et al., 2017; Comaills et al., 2016; Chi et al., 2022), nuclear envelope localized (Robijns et al., 2016; Vos et al., 2011; Vargas et al., 2012; Chen et al., 2018; Jung-Garcia et al., 2023), ER/nuclear membrane structure (Bahmanyar and Schlieker, 2020), and cytoskeleton (Tamiello et al., 2013; Takaki et al., 2017; Hatch and Hetzer, 2016; Pho et al., 2022), which were enriched overall in the screen (Fig. S3A). Following knockdown for 48 h, cells were arrested in S phase for 24 h, fixed, and labeled with Hoechst before imaging. The S phase arrest limited false positives from post-mitotic cells and enabled identification of factors that decreased rupture frequency with a high statistical confidence. The screen was conducted as at least three technical replicates using siRNA pools against LMNB1 and SUN1 as positive controls and a non-targeting siRNA pool in three wells as a negative control for each round (Fig. S3B). To calculate the nuclear rupture frequency for each condition, images were analyzed using the pipeline described in figure 2, the nuc:cyto RFP-Cyto mean intensity ratio calculated on cells passing all the filters, and results from all replicates were pooled and analyzed for significant difference compared to the pooled control wells by Barnard's test with Bonferroni correction for multiple hypothesis testing. An initial analysis of the distribution of the RFP-Cyto nuc:cyto ratio in our positive and negative control wells identified significant differences between these conditions (Fig. 3A), demonstrating that our screen design was sufficiently sensitive to identify biologically relevant changes in rupture frequency.

Precision/recall analysis of conditions with extreme values for nucleus size, solidity, and RFP-Cyto nuclear intensity indicated that quantifying the proportion of cells with a nuc:cyto ratio greater than one standard deviation above the median for each condition resulted in a robust quantification of cells with mislocalized RFP-Cyto with a precision of 93% and a recall of 90% (Fig. S3C). Analysis of segmentation errors in the same group of conditions found that the majority of cells were properly segmented in the post-filtering pool (Fig. S3C), indicating that our filters were set appropriately. Conditions that were significant outliers for RFP-Cyto ratio, nucleus morphology, or Hoechst intensity were manually checked. Through this analysis,

PSMC1 knockdown was determined to be uninterpretable due to excessive cell death, consistent with its function as an essential proteosome component (Fig. S3G).

Using an adjusted p-value cut-off of 0.05 and a fold-change cut-off of 0.3**,** 22 genes were identified as hits (24% of screen), with 14 (63.6%) decreasing rupture when depleted and 8 (36.4%) increasing it (Fig. 3B-C). To validate these results, we selected six hits to re-analyze for rupture frequency using single siRNAs to decrease the likelihood of off-target effects. Rupture frequency was analyzed by fixed cell analysis using the same experimental set up and analysis as the screen. We found that 6/6 targets significantly altered rupture frequency in the same direction as in the screen (Fig. 3D). These data demonstrate that our screen allows unbiased identification of nuclear membrane stability factors with a high degree of accuracy.

Changes in nucleus morphology are often strongly correlated with changes in nucleus stability (Srivastava et al., 2021). To determine how nucleus morphology correlated with nuclear rupture frequency in our dataset, we determined the median nuclear area and solidity for each condition and compared it to the rupture frequency. Our analysis identified known regulators of nucleus size (lamin B1 and CTDNEP1 depletion) validating the utility of our system for morphometric analysis (Fig. S3D-F). Correlation analysis found no significant relationship between nucleus rupture and nucleus area (Fig. 3E) suggesting that nucleus morphology is not a strong predictor of membrane stability within this gene set.

To determine whether specific pathways were enriched in regulators of nuclear membrane stability, we first assessed the frequency with which targeted or randomly selected genes affected rupture frequency. We found a slight enrichment of targeted genes in our hits, however, this enrichment was not significant (Fig. S4A), suggesting that a fully unbiased screen would be as successful as a larger targeted one in identifying key regulators. To determine whether specific pathways were over-represented in our hit list compared to our initial screen, we analyzed the hits for their functional properties using gene ontology (GO) term analyses and hypergeometric enrichment statistics. The most enriched GO groups were cytoskeletal organization and the nuclear membrane/ER network (Fig. 4A-B), both of which are known membrane stability regulation categories. In addition, we identified enrichment in unexpected transcriptional categories, including tissue development, demonstrating the power of this method to identify larger cellular changes that affect nuclear envelope homeostasis.

CTDNEP1 maintains nuclear membrane stability in interphase

A prominent group of factors affecting nuclear membrane stability both positively and negatively were those that regulated the structure of the ER and nuclear membrane, with one of these factors, CTDNEP1, having the largest effect on stability of any protein tested (Fig. 3C). This prompted us to further characterize the effect of CTDNEP1 depletion on interphase nuclear membrane rupture. CTDNEP1 is a protein phosphatase in the nuclear membrane that regulates lipid composition in the INM through activation of the phosphatidic acid phosphatase, lipin1 (Barger et al., 2021). Our initial validation found that transfection of a single siRNA against CTDNEP1 increased nucleus rupture frequency (Fig. 3D), and we confirmed that multiple single siRNAs resulted in substantial loss of the CTNDEP1 mRNA (Fig. 5B, Fig. S5A-B, Movie S3). Analysis of ER morphology in cells depleted of CTDNEP1 by labeling with antibodies against calreticulin found an increase in

ER area, as previously reported (Fig. 5A, (Merta et al., 2021)), consistent with loss of the protein. To confirm that mislocalization of RFP-Cyto to the nucleus after CTDNEP1 depletion is due to increased rupture frequency, we analyzed rupture frequency by live-cell imaging after transfecting U2OS-shLMNB1 cells with single control or CTDNEP1 siRNAs. We found that CTDNEP1 knockdown increased rupture frequency for both siRNAs tested in both U2OS and in HeLa cells (Fig. 5B, Fig. S5B), strongly suggesting that CTDNEP1 depletion has a specific effect on nuclear rupture frequency and that this effect is not cell-type specific. Previous work demonstrated that CTDNEP1 loss can impair nuclear membrane sealing (Penfield et al., 2020). To determine whether CTDNEP1 regulated nuclear membrane repair after rupture, we quantified rupture duration in U2OS RuptR cells after transfection with control or CTDNEP1 siRNAs. We found no significant increase in rupture duration (Fig. 5C), suggesting the main activity of CTDNEP1 is to stabilize the nuclear membrane and inhibit nuclear rupture.

Discussion

We have developed a reporter for transient interphase nuclear membrane rupture and a fully automated fixed-cell analysis that can rapidly and accurately identify conditions that alter rupture frequency. This ability allowed us to identify new cellular proteins that regulate nuclear membrane stability in an unbiased manner for the first time. This tool can be used in any system that allows exogenous protein expression and has a segmentable cytoplasm compartment. By eliminating the need for live-cell imaging, our new reporter system lowers the barrier of entry for cell biologists in any field to evaluate the contribution of nuclear membrane stability to their phenotype of interest. In addition to identifying new regulators, our development of a robust fixed-cell nuclear rupture reporter and analysis pipeline allows rapid analysis of nuclear membrane stability for tens of conditions in a single day. This enables for the first time in-depth analyses of genetic interactions and critical domains in proteins of interest and accurate analysis of conditions that are not amenable to long-term live-cell imaging, including timing analyses. Expression of a single construct and optimization of a few thresholds in the analysis pipeline enables any cell line to be analyzed and the use of fixed cells and robust filters to exclude mitosis and cell death events enables changes in rupture frequency to be identified in asynchronous or highly motile cells with a high degree of sensitivity.

Our initial siRNA screen against targeted and randomly selected genes reported here had a high hit and validation rate for both groups. This high success rate strongly suggests that nuclear membrane stability is exquisitely sensitive to changes in nuclear envelope structure and can be used to identify new structural regulators from broad functional groups. Our results support a significant role for membrane structural proteins in determining rupture frequency. Of the proteins driving GO:Cellular Component enrichment in nuclear/ER membrane categories, the majority regulate the physical structure of the membranes, including ones that regulate ER morphology (LNPK, CTDNEP1) (Chen et al., 2012; Bahmanyar et al., 2014; Wang et al., 2016; Zhou et al., 2019; Merta et al., 2021; Peterson et al., 2011), nuclear pore membrane structure (NDC1)(Hampoelz et al., 2019), and lipid composition (EVOLV1, CTDNEP1)(Kim et al., 2007; Han et al., 2012; Leonard et al., 2004; Jakobsson et al., 2006). A major gap in our understanding of nuclear membrane rupture is how the membrane responds to mechanical stress. Several lipid-based mechanisms could relieve nuclear

membrane tension and prevent loss of nucleus integrity. These mechanisms include increasing membrane flow through ER/NE and NPC junctions, altering lipid metabolism and transport to favor lipids that mitigate tension, or increasing lipid synthesis. Each of these pathways has been documented in other cellular membranes or other organisms and have representative proteins present in mammalian nuclei (Cornell, 2016; Haider et al., 2018; Kinugasa et al., 2019; Hirano et al., 2020; Lee et al., 2022; Witkin et al., 2012; Santos-Rosa et al., 2005; Siniossoglou, 2013; Roux et al., 2019), but whether these activities are critical for nuclear membrane stability in mammalian cells is unknown.

CTDNEP1 is one such factor that regulates fatty acid synthesis and nuclear membrane lipid composition through activation of the phosphatidic acid phosphatase, lipin1 (Peterson et al., 2011; Merta et al., 2021; Siniossoglou et al., 1998; Kim et al., 2007; Santos-Rosa et al., 2005; Han et al., 2012). CTDNEP1 affects several aspects of nuclear structure, including proper chromosome segregation and post-mitotic resealing, nuclear pore insertion, actin organization, nuclear envelope protein composition, and nuclear size (Lee et al., 2022; Merta et al., 2021; Penfield et al., 2020; Bahmanyar et al., 2014; Jacquemyn et al., 2021; Calero-Cuenca et al., 2021; Krshnan et al., 2022). CTDNEP1 is one of a broad group of proteins assessed in our screen that increased nucleus size upon depletion, which we expected to increase resistance to mechanical stress (Lomakin et al., 2020; Venturini et al., 2020; Berre et al., 2012). However, large nucleus size did not correlate with lower rupture frequency (Fig. 3E), suggesting membrane quantity is only one in a complex network of pathways determining nuclear membrane tension. Inactivation of CTDNEP1 is also proposed to cause misregulation of major signaling pathways, including myc, BMP and WNT (Hayata et al., 2018; Darrigrand et al., 2020; Satow et al., 2006; Tanaka et al., 2013; Sakaguchi et al., 2013; Luo et al., 2023). Determining how CTDNEP1 regulates nuclear membrane stability will further define the function of local lipid metabolism in NE structure and could elucidate a new molecular mechanism for broad signaling disruption upon its loss.

In this study we focused on broadly identifying proteins that regulate nuclear membrane rupture frequency in a well-characterized reporter cell line. We anticipate that ongoing improvements to the RFP-Cyto reporter pipeline and combining it with additional reporters and morphometric analyses will allow proteins at even more steps in the rupture and repair process to be identified in even more *in vivo*-like conditions. For instance, adding an analysis of GFP-Nuc localization to this pipeline will allow proteins that disrupt nuclear repair, such as BAF, to be identified. Also, adding an analysis of membrane curvature could identify proteins that unlink rupture from membrane blebs, providing new insight into how membrane interactions with the nuclear lamina becomes destabilized (Stephens et al., 2017; Berg et al., 2022; Chen et al., 2018; Srivastava et al., 2021). Overall, the ability to rapidly screen for and quantify changes in nuclear rupture frequency will lead to new insights into the molecular mechanisms regulating NE structure and dynamics.

Methods

Cell lines and transfection

U2OS (ATCC:HTB-96) and HeLa (ATCC:CCL-2)cells were grown in 1x DMEM (GIBCO) plus 10% FBS (Sigma-Aldrich), 1% Penicillin-Streptomycin (GIBCO) at 10% CO_2 and 5% CO_2 respectively. U2OS shLMNB1 RFP-NLS cells were characterized previously (Young et al., 2020). siRNAs were transfected using siLentfect (Bio-Rad Laboratories) according to the manufacturer's instructions and cells were analyzed at least 72 h post-transfection. RFP-cyto was introduced by stable transduction into U2OS shLMNB1 GFP-NLS lines characterized previously in (Hatch and Hetzer, 2016). U2OS cells were arrested in S phase by a single addition of 2 mM thymidine (Sigma-Aldrich), diluted fresh in PBS, 24 h before and for the duration of imaging. HeLa cells were arrested in S phase by a single addition of 2 mM hydroxyurea (EMD Millipore) diluted in water. Cell lines were validated by STR fingerprinting performed by an on campus shared resource.

Plasmids and siRNAs

pLVXE-Blast::mCherry-TagRFP-Luciferase (RFP-cyto) was constructed by traditional cloning to insert mCherry-TagRFP-Luciferase into the pLVXE lentiviral vector following an EF1a core promoter.

Known siRNA validation: siRNAs against CTRL (non-targeting, cat#: D-001810-01-05), LMNA (5'-GGUGGUGACGAUCUGGGCUuu-3'), LMNB1 (5'-CGCGCUUGGUAGAGGUGGAUUuu-3'), and SUN1 (5'-ACCAGGUGCCUUCGAAAuu-3') purchased from Horizon Discovery. Cells were left in 35 nM transfection medium for 48 h.

siRNA screen: ON-TARGETplus SmartPool siRNAs were purchased in a 96-well plate from Horizon Discovery according to Table S1. U2OS cells were left in 35 nM transfection media 48 h.

Single siRNA validation: ON-TARGETplus siRNAs were purchased from Horizon Discovery. Individual siRNAs were transfected at 35 nM into U2OS cells for 48 h and assessed after 72 h. siRNAs: CTRL (cat#: D-001810-01-05), RASA1 (cat#: J-005276-07), NRM (cat#: J-012779-22), ARID4A (cat#: J-003949-05), NDC1 (5'-CUGCACCACAGUAUUUAUAUU-3'), CTDNEP1 (cat#: J-017869-09), MYCBP2 (cat#: J-006951-05).

CTDNEP1: siRNAs were purchased from Horizon Discovery for CTDNEP1-9 (cat#: J-017869-09), and CTDNEP1-10 (cat#: J-017869-09). Non targeting siRNA (above) was used as a control. siRNAs were transfected in50 nM transfection medium and left on overnight (U2OS), or 5 h (HeLa).

Fixed Cell Imaging

Samples fixed 45 min in 4% paraformaldehyde (Electron Microscopy Sciences) in PBS were stained 20 min 1ug/mL Hoechst (Life Technologies) and imaged as single confocal slices via 40x/0.75 Plan Apo objective on Leica DMi8 with a Yokogawa CSU spinning disc, Andor Borealis illumination and an ASI automated stage with Piezo Z-axis. Images were captured with an Andor iXon Ultra 888 EMCCD camera using MetaMorph software (version 7.10.4; Molecular Devices) equipped with a plate acquisition journal. Images were corrected for background signal prior to measurements and image displays exhibit rescaled intensity as noted in the CellProfiler pipeline or modified for brightness/contrast in ImageJ.

Time-lapse imaging

Time lapse images are single confocal slices captured with Leica DMi8 spinning disk microscope and 40x/0.75 Plan Apo objective, described in Fixed Cell Imaging, at 3 m intervals over 18-24 h. Image sequences were adjusted for brightness and contrast using ImageJ.

Immunofluorescence

For indirect immunofluorescence of calreticulin, U2OS cells were grown on glass coverslips and fixed 10 min in methanol at −20°C and rehydrated 10 min in PBS at RT. Coverslips were blocked in 3% BSA in PBS plus 0.4% Triton X-100 for 30 min at RT and incubated in primary antibody rabbit anti–Calreticulin at 1:100 (Cell Signaling Technology) overnight at 4°C. Goat anti rabbit Alexa Fluor647 (Thermo Fisher Scientific) secondary antibody diluted in blocking buffer 1:1000 and used for 30 min at RT. Coverslips were then briefly incubated in 1 µg/ml DAPI in PBS (Roche) and mounted in Vectashield (Vector Laboratories).

Confocal z-stacks were acquired with a Leica TCS SP8 confocal microscope with a Leica HCX Plan Apo 63x/1.40 Oil CS2 objective with a z-step size of 0.15 µm. Post-acquisition, images were deconvolved using Lightning through the LAS X software. Images are single confocal sections. Images were adjusted for brightness and contrast using ImageJ.

qRT-PCR

Cells were harvested from a confluent well in a 6-well plate with 0.25% Trypsin-EDTA, pelleted, and frozen at -80°C. RNA was extracted using RNeasy Mini Plus kit (Qiagen) following manufacturer's instruction. cDNA was synthesized using iScript RT Supermix (BioRad). A 5ng/ul cDNA reaction mix was set up according to manufacturer's instructions (SYBR green MM, Fisher Scientific). Thermal cycling was performed at 50°C for 2 min then 95°C for 10 min then 40 cycles of 95°C for 15s, 60°C for 60 s QuantStudio™ 5 Real-Time PCR System (ThermoFisher). Oligo sequences: 5'- AACAGCCTCAAGATCATCAGC -3' (GAPDH forward), 5'-AGGAGCCATCCAGACAATGC-3' (CTDNEP1 forward), 5'- CACCACCTTCTTGATGTCATC-3' (GAPDH reverse), 5'- TCAGCACGGAACGAACATCA-3' (CTDNEP1 reverse). Ct values for CTDNEP1 were normalized internally to GAPDH and then to transcript levels in cells treated with non-targeting siRNA.

Statistics and quantification

Quantification of fixed image data generated by CellProfiler 4.2.4: Images corrected for background signal were analyzed for mean intensity RFP and GFP in the nucleus and cytoplasm using mask objects generated by rescaling intensity, downsampling, median filtering, and adaptive Otsu thresholding of Hoechst (nucleus) and RFP (cytoplasm). Morphological measurements of the nucleus used for data filtering and comparisons were generated from the Hoechst mask. Rupture frequency for fixed images was determined either by data output from CellProfiler, in which rupture was determined if the nuclear to cytoplasmic ratio of RFP exceeded one standard deviation above the median for the experimental control, or manually (as noted for validation)

based on visual identification of nuclear RFP signal. Intensity outputs from CellProfiler were measured from eroded masks to reduce error from oversegmentation.

Quantification of rupture frequency and duration in time-lapse image analysis was done manually in ImageJ by visually identifying a rapid loss of compartmentalization and subsequent restoration of nuclear localization signal, as previously done (Young et al., 2020).

Hypergeometric enrichment analysis was completed in R using the mysigdbr and clusterProfiler packages. For enrichment of statistically significant rupture frequency hits within the context of the screen, gene sets from the Broad Institute C5:GO database were first joined to the complete gene list for the siRNA screen, ensuring hit enrichment calculations were performed relative to the landscape of the screen. Enrichment scores were determined by dividing the gene ratio by the background ratio, and p-values determined by Fishers exact test as generated by the enricher function (enricher(gene = hits, TERM2GENE = screen)).

All statistic tests were conducted using R (version 4.2.1). Each dataset completed with a minimum of 3 biological replicates unless otherwise noted. Pair-wise comparisons on categorical data were analyzed using Barnard's exact test ("Barnard" package, R), comparing non-gaussian distributions utilized Wilcoxon rank sum test (base R), Bonferroni or false discovery rate correction for multiple testing applied as indicated for statistical analyses with greater than five comparisons.

Acknowledgments
E.M.H, A.L.G., and A.Y. were supported by the National Institutes of Health grant R35GM124766. This work was supported by the Cellular Imaging and Flow Cytometry Shared Resources of the Fred Hutch/University of Washington Cancer Consortium (P30 CA015704) and Fred Hutch Scientific Computing, NIH grants S10-OD-020069 and S10-OD-028685. Schematics were generated with BioRender.com.

Author Contributions
AL Gunn: conceptualization, data curation, formal analysis, investigation, methodology, project administration, validation, visualization, writing – original draft, review and editing
A Yashchenko: data curation, formal analysis, investigation, methodology, visualization, writing – review and editing
EM Hatch: conceptualization, formal analysis, funding acquisition, investigation, methodology, project administration, resources, supervision, visualization, writing – original draft, review & editing

Conflict of Interest Statement
The authors declare that they have no conflict of interest.

References

Aureille, J., V. Buffière-Ribot, B.E. Harvey, C. Boyault, L. Pernet, T. Andersen, G. Bacola, M. Balland, S. Fraboulet, L.V. Landeghem, and C. Guilluy. 2019. Nuclear envelope deformation controls cell cycle progression in response to mechanical force. *EMBO reports*. 20:e48084. doi:10.15252/embr.201948084.

Bahmanyar, S., R. Biggs, A.L. Schuh, A. Desai, T. Müller-Reichert, A. Audhya, J.E. Dixon, and K. Oegema. 2014. Spatial control of phospholipid flux restricts endoplasmic reticulum sheet formation to allow nuclear envelope breakdown. *Genes & development*. 28:121–126. doi:10.1101/gad.230599.113.

Bahmanyar, S., and C. Schlieker. 2020. Lipid and protein dynamics that shape nuclear envelope identity. *Mol Biol Cell*. 31:1315–1323. doi:10.1091/mbc.e18-10-0636.

Barger, S.R., L. Penfield, and S. Bahmanyar. 2021. Coupling lipid synthesis with nuclear envelope remodeling. *Trends Biochem Sci*. 47:52–65. doi:10.1016/j.tibs.2021.08.009.

Berg, I.K., M.L. Currey, S. Gupta, Y. Berrada, B.N. Viet, M. Pho, A.E. Patteson, J.M. Schwarz, E.J. Banigan, and A.D. Stephens. 2022. Transcription regulates bleb formation and stability independent of nuclear rigidity. doi:10.1101/2022.11.14.516344.

Berre, M.L., J. Aubertin, and M. Piel. 2012. Fine control of nuclear confinement identifies a threshold deformation leading to lamina rupture and induction of specific genes. *Integrative biology : quantitative biosciences from nano to macro*. 4:1406–1414. doi:10.1039/c2ib20056b.

Calero-Cuenca, F.J., D.S. Osorio, S. Carvalho-Marques, S.C. Sridhara, L.M. Oliveira, Y. Jiao, J. Diaz, C.S. Janota, B. Cadot, and E.R. Gomes. 2021. Ctdnep1 and Eps8L2 regulate dorsal actin cables for nuclear positioning during cell migration. *Curr Biol*. 31:1521-1530.e8. doi:10.1016/j.cub.2021.01.007.

Carpenter, A.E., T.R. Jones, M.R. Lamprecht, C. Clarke, I.H. Kang, O. Friman, D.A. Guertin, J.H. Chang, R.A. Lindquist, J. Moffat, P. Golland, and D.M. Sabatini. 2006. CellProfiler: image analysis software for identifying and quantifying cell phenotypes. *Genome biology*. 7:R100. doi:10.1186/gb-2006-7-10-r100.

Chen, N.Y., P. Kim, T.A. Weston, L. Edillo, Y. Tu, L.G. Fong, and S.G. Young. 2018. Fibroblasts lacking nuclear lamins do not have nuclear blebs or protrusions but nevertheless have frequent nuclear membrane ruptures. *Proceedings of the National Academy of Sciences of the United States of America*. 115:10100–10105. doi:10.1073/pnas.1812622115.

Chen, N.Y., P.H. Kim, Y. Tu, Y. Yang, P.J. Heizer, S.G. Young, and L.G. Fong. 2021. Increased expression of LAP2β eliminates nuclear membrane ruptures in nuclear lamin–deficient neurons and fibroblasts. *Proc National Acad Sci*. 118:e2107770118. doi:10.1073/pnas.2107770118.

Chen, N.Y., Y. Yang, T.A. Weston, J.N. Belling, P. Heizer, Y. Tu, P. Kim, L. Edillo, S.J. Jonas, P.S. Weiss, L.G. Fong, and S.G. Young. 2019. An absence of lamin B1 in migrating neurons causes nuclear membrane ruptures and cell death. *Proceedings of the National Academy of Sciences of the United States of America*. 116:25870–25879. doi:10.1073/pnas.1917225116.

Chen, S., P. Novick, and S. Ferro-Novick. 2012. ER network formation requires a balance of the dynamin-like GTPase Sey1p and the Lunapark family member Lnp1p. *Nat Cell Biol*. 14:707–716. doi:10.1038/ncb2523.

Chi, Y.-H., W.-P. Wang, M.-C. Hung, G.-G. Liou, J.-Y. Wang, and P.-H.G. Chao. 2022. Deformation of the nucleus by TGFβ1 via the remodeling of nuclear envelope and histone isoforms. *Epigenet Chromatin*. 15:1. doi:10.1186/s13072-021-00434-3.

Cho, S., M. Vashisth, A. Abbas, S. Majkut, K. Vogel, Y. Xia, I.L. Ivanovska, J. Irianto, M. Tewari, K. Zhu, E.D. Tichy, F. Mourkioti, H.-Y. Tang, R.A. Greenberg, B.L. Prosser, and D.E. Discher. 2019. Mechanosensing by the Lamina Protects against Nuclear Rupture, DNA Damage, and Cell-Cycle Arrest. *Developmental Cell*. doi:10.1016/j.devcel.2019.04.020.

Comaills, V., L. Kabeche, R. Morris, R. Buisson, M. Yu, M.W. Madden, J.A. LiCausi, M. Boukhali, K. Tajima, S. Pan, N. Aceto, S. Sil, Y. Zheng, T. Sundaresan, T. Yae, N.V. Jordan, D.T. Miyamoto, D.T. Ting, S. Ramaswamy, W. Haas, L. Zou, D.A. Haber, and S. Maheswaran. 2016. Genomic Instability Is Induced by Persistent Proliferation of Cells Undergoing Epithelial-to-Mesenchymal Transition. *Cell reports*. 17:2632–2647. doi:10.1016/j.celrep.2016.11.022.

Cornell, R.B. 2016. Membrane lipid compositional sensing by the inducible amphipathic helix of CCT. *Biochimica Et Biophysica Acta Bba - Mol Cell Biology Lipids*. 1861:847–861. doi:10.1016/j.bbalip.2015.12.022.

Cuylen-Haering, S., M. Petrovic, A. Hernandez-Armendariz, M.W.G. Schneider, M. Samwer, C. Blaukopf, L.J. Holt, and D.W. Gerlich. 2020. Chromosome clustering by Ki-67 excludes cytoplasm during nuclear assembly. *Nature*. 587:285–290. doi:10.1038/s41586-020-2672-3.

Darrigrand, J.-F., M. Valente, G. Comai, P. Martinez, M. Petit, R. Nishinakamura, D.S. Osorio, G. Renault, C. Marchiol, V. Ribes, and B. Cadot. 2020. Dullard-mediated Smad1/5/8 inhibition controls mouse cardiac neural crest cells condensation and outflow tract septation. *Elife*. 9:e50325. doi:10.7554/elife.50325.

Denais, C.M., R.M. Gilbert, P. Isermann, A.L. McGregor, M.T. Lindert, B. Weigelin, P.M. Davidson, P. Friedl, K. Wolf, and J. Lammerding. 2016. Nuclear envelope rupture and repair during cancer cell migration. *Science*. 352:aad7297-358. doi:10.1126/science.aad7297.

Earle, A.J., T.J. Kirby, G.R. Fedorchak, P. Isermann, J. Patel, S. Iruvanti, S.A. Moore, G. Bonne, L.L. Wallrath, and J. Lammerding. 2020. Mutant lamins cause nuclear envelope rupture and DNA damage in skeletal muscle cells. *Nature materials*. 19:464–473. doi:10.1038/s41563-019-0563-5.

Guey, B., M. Wischnewski, A. Decout, K. Makasheva, M. Kaynak, M.S. Sakar, B. Fierz, and A. Ablasser. 2020. BAF restricts cGAS on nuclear DNA to prevent innate immune activation. *Science*. 369:823–828. doi:10.1126/science.aaw6421.

Guscott, M., A. Saha, J. Maharaj, and S.E. McClelland. 2022. The Multifaceted Role of Micronuclei in Tumour Progression: A whole organism perspective. *Int J Biochem Cell Biology*. 106300. doi:10.1016/j.biocel.2022.106300.

Haider, A., Y.-C. Wei, K. Lim, A.D. Barbosa, C.-H. Liu, U. Weber, M. Mlodzik, K. Oras, S. Collier, M.M. Hussain, L. Dong, S. Patel, A. Alvarez-Guaita, V. Saudek, B.J. Jenkins, A. Koulman, M.K. Dymond, R.C. Hardie, S. Siniossoglou, and D.B. Savage. 2018. PCYT1A Regulates Phosphatidylcholine Homeostasis from the Inner Nuclear Membrane in Response to Membrane Stored Curvature Elastic Stress. *Dev Cell*. 45:481-495.e8. doi:10.1016/j.devcel.2018.04.012.

Halfmann, C.T., R.M. Sears, A. Katiyar, B.W. Busselman, L.K. Aman, Q. Zhang, C.S. O'Bryan, T.E. Angelini, T.P. Lele, and K.J. Roux. 2019. Repair of nuclear ruptures requires barrier-to-autointegration factor. *Journal of Cell Biology*. 114:jcb.201901116. doi:10.1083/jcb.201901116.

Hampoelz, B., A. Andres-Pons, P. Kastritis, and M. Beck. 2019. Structure and Assembly of the Nuclear Pore Complex. *Annu Rev Biophys*. 48:1–22. doi:10.1146/annurev-biophys-052118-115308.

Han, S., S. Bahmanyar, P. Zhang, N. Grishin, K. Oegema, R. Crooke, M. Graham, K. Reue, J.E. Dixon, and J.M. Goodman. 2012. Nuclear envelope phosphatase 1-regulatory subunit 1 (formerly TMEM188) is the

metazoan Spo7p ortholog and functions in the lipin activation pathway. *Journal of Biological Chemistry*. 287:3123–3137. doi:10.1074/jbc.m111.324350.

Hatch, E.M., A.H. Fischer, T.J. Deerinck, and M.W. Hetzer. 2013. Catastrophic nuclear envelope collapse in cancer cell micronuclei. *Cell*. 154:47–60. doi:10.1016/j.cell.2013.06.007.

Hatch, E.M., and M.W. Hetzer. 2016. Nuclear envelope rupture is induced by actin-based nucleus confinementActin-based nuclear envelope rupture. *J Cell Biology*. 215:27–36. doi:10.1083/jcb.201603053.

Hayata, T., M. Chiga, Y. Ezura, M. Asashima, H. Katabuchi, R. Nishinakamura, and M. Noda. 2018. Dullard deficiency causes hemorrhage in the adult ovarian follicles. *Genes Cells*. 23:345–356. doi:10.1111/gtc.12575.

Hirano, Y., Y. Kinugasa, H. Osakada, T. Shindo, Y. Kubota, S. Shibata, T. Haraguchi, and Y. Hiraoka. 2020. Lem2 and Lnp1 maintain the membrane boundary between the nuclear envelope and endoplasmic reticulum. *Communications biology*. 3:276–14. doi:10.1038/s42003-020-0999-9.

Houben, F., W.H.D. Vos, I.P.C. Krapels, M. Coorens, G.J.J. Kierkels, M.A.F. Kamps, V.L.R.M. Verstraeten, C.L.M. Marcelis, A. van den Wijngaard, F.C.S. Ramaekers, and J.L.V. Broers. 2013. Cytoplasmic localization of PML particles in laminopathies. *Histochemistry and Cell Biology*. 139:119–134. doi:10.1007/s00418-012-1005-5.

Irianto, J., Y. Xia, C.R. Pfeifer, A. Athirasala, J. Ji, C. Alvey, M. Tewari, R.R. Bennett, S.M. Harding, A.J. Liu, R.A. Greenberg, and D.E. Discher. 2017. DNA Damage Follows Repair Factor Depletion and Portends Genome Variation in Cancer Cells after Pore Migration. *Current biology*. 27:210–223. doi:10.1016/j.cub.2016.11.049.

Jacquemyn, J., J. Foroozandeh, K. Vints, J. Swerts, P. Verstreken, N.V. Gounko, S.F. Gallego, and R. Goodchild. 2021. Torsin and NEP1R1-CTDNEP1 phosphatase affect interphase nuclear pore complex insertion by lipid-dependent and lipid-independent mechanisms. *Embo J*. 40:e106914. doi:10.15252/embj.2020106914.

Jakobsson, A., R. Westerberg, and A. Jacobsson. 2006. Fatty acid elongases in mammals: Their regulation and roles in metabolism. *Prog Lipid Res*. 45:237–249. doi:10.1016/j.plipres.2006.01.004.

Jung-Garcia, Y., O. Maiques, J. Monger, I. Rodriguez-Hernandez, B. Fanshawe, M.-C. Domart, M.J. Renshaw, R.M. Marti, X. Matias-Guiu, L.M. Collinson, V. Sanz-Moreno, and J.G. Carlton. 2023. LAP1 supports nuclear adaptability during constrained melanoma cell migration and invasion. *Nat Cell Biol*. 1–12. doi:10.1038/s41556-022-01042-3.

Kim, P.H., N.Y. Chen, P.J. Heizer, Y. Tu, T.A. Weston, J.L.-C. Fong, N.K. Gill, A.C. Rowat, S.G. Young, and L.G. Fong. 2021. Nuclear membrane ruptures underlie the vascular pathology in a mouse model of Hutchinson-Gilford progeria syndrome. *Jci Insight*. 6:e151515. doi:10.1172/jci.insight.151515.

Kim, Y., M.S. Gentry, T.E. Harris, S.E. Wiley, J.C. Lawrence, and J.E. Dixon. 2007. A conserved phosphatase cascade that regulates nuclear membrane biogenesis. *Proc National Acad Sci*. 104:6596–6601. doi:10.1073/pnas.0702099104.

King, M.C., and C.P. Lusk. 2016. A model for coordinating nuclear mechanics and membrane remodeling to support nuclear integrity. *Current Opinion in Cell Biology*. 41:9–17. doi:10.1016/j.ceb.2016.03.009.

Kinugasa, Y., Y. Hirano, M. Sawai, Y. Ohno, T. Shindo, H. Asakawa, Y. Chikashige, S. Shibata, A. Kihara, T. Haraguchi, and Y. Hiraoka. 2019. The very-long-chain fatty acid elongase Elo2 rescues lethal defects associated with loss of the nuclear barrier function in fission yeast cells. *Journal of cell science*. 132:jcs229021. doi:10.1242/jcs.229021.

Krshnan, L., W.S. Siu, M.V. de Weijer, D. Hayward, E.N. Guerrero, U. Gruneberg, and P. Carvalho. 2022. Regulated degradation of the inner nuclear membrane protein SUN2 maintains nuclear envelope architecture and function. *Elife*. 11. doi:10.7554/elife.81573.

Krupina, K., A. Goginashvili, and D.W. Cleveland. 2021. Causes and consequences of micronuclei. *Curr Opin Cell Biol*. 70:91–99. doi:10.1016/j.ceb.2021.01.004.

Lee, S., H. Merta, J.W.C. Rodríguez, and S. Bahmanyar. 2022. A membrane sensing mechanism couples local lipid metabolism to protein degradation at the inner nuclear membrane. *Biorxiv*. 2022.07.06.498903. doi:10.1101/2022.07.06.498903.

Leonard, A.E., S.L. Pereira, H. Sprecher, and Y.-S. Huang. 2004. Elongation of long-chain fatty acids. *Prog Lipid Res*. 43:36–54. doi:10.1016/s0163-7827(03)00040-7.

Lomakin, A.J., C.J. Cattin, D. Cuvelier, Z. Alraies, M. Molina, G.P.F. Nader, N. Srivastava, P.J. Saez, J.M. Garcia-Arcos, I.Y. Zhitnyak, A. Bhargava, M.K. Driscoll, E.S. Welf, R. Fiolka, R.J. Petrie, N.S.D. Silva, J.M. González-Granado, N. Manel, A.M. Lennon-Duménil, D.J. Müller, and M. Piel. 2020. The nucleus acts as a ruler tailoring cell responses to spatial constraints. *Science (New York, N.Y.)*. 370. doi:10.1126/science.aba2894.

Luo, Z., D. Xin, Y. Liao, K. Berry, S. Ogurek, F. Zhang, L. Zhang, C. Zhao, R. Rao, X. Dong, H. Li, J. Yu, Y. Lin, G. Huang, L. Xu, M. Xin, R. Nishinakamura, J. Yu, M. Kool, S.M. Pfister, M.F. Roussel, W. Zhou, W.A. Weiss, P. Andreassen, and Q.R. Lu. 2023. Loss of phosphatase CTDNEP1 potentiates aggressive medulloblastoma by triggering MYC amplification and genomic instability. *Nat Commun*. 14:762. doi:10.1038/s41467-023-36400-8.

MacDonald, K.M., S. Nicholson-Puthenveedu, M.M. Tageldein, S. Khasnis, C.H. Arrowsmith, and S.M. Harding. 2023. Antecedent chromatin organization determines cGAS recruitment to ruptured micronuclei. *Nat Commun*. 14:556. doi:10.1038/s41467-023-36195-8.

Maciejowski, J., and E.M. Hatch. 2020. Nuclear Membrane Rupture and Its Consequences. *Annu Rev Cell Dev Bi*. 36:1–30. doi:10.1146/annurev-cellbio-020520-120627.

Maciejowski, J., Y. Li, N. Bosco, P.J. Campbell, and T. de Lange. 2015. Chromothripsis and Kataegis Induced by Telomere Crisis. *Cell*. 163:1641–1654. doi:10.1016/j.cell.2015.11.054.

Maurer, M., and J. Lammerding. 2019. The Driving Force: Nuclear Mechanotransduction in Cellular Function, Fate, and Disease. *Annu Rev Biomed Eng*. 21:1–26. doi:10.1146/annurev-bioeng-060418-052139.

Merta, H., J.W.C. Rodríguez, M.I. Anjur-Dietrich, T. Vitale, M.E. Granade, T.E. Harris, D.J. Needleman, and S. Bahmanyar. 2021. Cell cycle regulation of ER membrane biogenesis protects against chromosome missegregation. *Dev Cell*. 56:3364-3379.e10. doi:10.1016/j.devcel.2021.11.009.

Nader, G.P. de F., S. Agüera-Gonzalez, F. Routet, M. Gratia, M. Maurin, V. Cancila, C. Cadart, A. Palamidessi, R.N. Ramos, M.S. Roman, M. Gentili, A. Yamada, A. Williart, C. Lodillinsky, E. Lagoutte, C. Villard, J.-L. Viovy, C. Tripodo, J. Galon, G. Scita, N. Manel, P. Chavrier, and M. Piel. 2021a. Compromised nuclear envelope integrity drives TREX1-dependent DNA damage and tumor cell invasion. *Cell*. 184:5230-5246.e22. doi:10.1016/j.cell.2021.08.035.

Nader, G.P. de F., A. Williart, and M. Piel. 2021b. Nuclear deformations, from signaling to perturbation and damage. *Curr Opin Cell Biol*. 72:137–145. doi:10.1016/j.ceb.2021.07.008.

Niethammer, P. 2021. Components and Mechanisms of Nuclear Mechanotransduction. *Annu Rev Cell Dev Bi*. 37:1–24. doi:10.1146/annurev-cellbio-120319-030049.

Noronha, C.M. de, M.P. Sherman, H.W. Lin, M.V. Cavrois, R.D. Moir, R.D. Goldman, and W.C. Greene. 2001. Dynamic disruptions in nuclear envelope architecture and integrity induced by HIV-1 Vpr. *Science*. 294:1105–1108. doi:10.1126/science.1063957.

Penfield, L., R. Shankar, E. Szentgyörgyi, A. Laffitte, M.S. Mauro, A. Audhya, T. Müller-Reichert, and S. Bahmanyar. 2020. Regulated lipid synthesis and LEM2/CHMP7 jointly control nuclear envelope closure. *Journal of Cell Biology*. 219:15. doi:10.1083/jcb.201908179.

Penfield, L., B. Wysolmerski, M. Mauro, R. Farhadifar, M.A. Martinez, R. Biggs, H.-Y. Wu, C. Broberg, D. Needleman, and S. Bahmanyar. 2018. Dynein-pulling forces counteract lamin-mediated nuclear stability during nuclear envelope repair. *Mol Biol Cell*. 29:mbc.E17-06-0374. doi:10.1091/mbc.e17-06-0374.

Peterson, T.R., S.S. Sengupta, T.E. Harris, A.E. Carmack, S.A. Kang, E. Balderas, D.A. Guertin, K.L. Madden, A.E. Carpenter, B.N. Finck, and D.M. Sabatini. 2011. mTOR Complex 1 Regulates Lipin 1 Localization to Control the SREBP Pathway. *Cell*. 146:408–420. doi:10.1016/j.cell.2011.06.034.

Pfleghaar, K.B., P. Taimen, V. Butin-Israeli, T. Shimi, S. Langer-Freitag, Y. Markaki, A.E. Goldman, M. Wehnert, and R.D. Goldman. 2015. Gene-rich chromosomal regions are preferentially localized in the lamin B deficient nuclear blebs of atypical progeria cells. *Nucleus*. 6:66–76. doi:10.1080/19491034.2015.1004256.

Pho, M., Y. Berrada, A. Gunda, A. Lavallee, K. Chiu, A. Padam, M.L. Currey, and A.D. Stephens. 2022. Actin contraction controls nuclear blebbing and rupture independent of actin confinement. *Biorxiv*. 2022.12.01.518663. doi:10.1101/2022.12.01.518663.

Raab, M., M. Gentili, H. de Belly, H.R. Thiam, P. Vargas, A.J. Jimenez, F. Lautenschlaeger, R. Voituriez, A.M. Lennon-Duménil, N. Manel, and M. Piel. 2016. ESCRT III repairs nuclear envelope ruptures during cell migration to limit DNA damage and cell death. *Science*. 352:aad7611-362. doi:10.1126/science.aad7611.

Robijns, J., F. Molenberghs, T. Sieprath, T.D.J. Corne, M. Verschuuren, and W.H.D. Vos. 2016. In silico synchronization reveals regulators of nuclear ruptures in lamin A/C deficient model cells. *Scientific Reports*. 6:30325. doi:10.1038/srep30325.

Roux, A.-L.L., X. Quiroga, N. Walani, M. Arroyo, and P. Roca-Cusachs. 2019. The plasma membrane as a mechanochemical transducer. *Philosophical Transactions Royal Soc B*. 374:20180221. doi:10.1098/rstb.2018.0221.

Sakaguchi, M., S. Sharmin, A. Taguchi, T. Ohmori, S. Fujimura, T. Abe, H. Kiyonari, Y. Komatsu, Y. Mishina, M. Asashima, E. Araki, and R. Nishinakamura. 2013. The phosphatase Dullard negatively regulates BMP signalling and is essential for nephron maintenance after birth. *Nat Commun*. 4:1398. doi:10.1038/ncomms2408.

Samwer, M., M.W.G. Schneider, R. Hoefler, P.S. Schmalhorst, J.G. Jude, J. Zuber, and D. Gerlich. 2017. DNA Cross-Bridging Shapes a Single Nucleus from a Set of Mitotic Chromosomes. *Cell*. 170:956-972.e23. doi:10.1016/j.cell.2017.07.038.

Santos-Rosa, H., J. Leung, N. Grimsey, S. Peak-Chew, and S. Siniossoglou. 2005. The yeast lipin Smp2 couples phospholipid biosynthesis to nuclear membrane growth. *EMBO Journal*. 24:1931–1941. doi:10.1038/sj.emboj.7600672.

Satow, R., A. Kurisaki, T. Chan, T.S. Hamazaki, and M. Asashima. 2006. Dullard Promotes Degradation and Dephosphorylation of BMP Receptors and Is Required for Neural Induction. *Dev Cell*. 11:763–774. doi:10.1016/j.devcel.2006.10.001.

Shah, P., C.M. Hobson, S. Cheng, M.J. Colville, M.J. Paszek, R. Superfine, and J. Lammerding. 2020. Nuclear Deformation Causes DNA Damage by Increasing Replication Stress. *Curr Biol*. doi:10.1016/j.cub.2020.11.037.

Shimi, T., K. Pfleghaar, S. Kojima, C.-G. Pack, I. Solovei, A.E. Goldman, S.A. Adam, D.K. Shumaker, M. Kinjo, T. Cremer, and R.D. Goldman. 2008. The A- and B-type nuclear lamin networks: microdomains involved in chromatin organization and transcription. *Genes & development*. 22:3409–3421. doi:10.1101/gad.1735208.

Silva, N.S.D., G.P.F. Nader, F. Nadalin, K. de Azevedo, M. Couty, A. Bhargava, C. Conrad, M. Maurin, C. Fouillade, A. Londono-Vallejo, R. Behrendt, L. Gallwitz, P. Saftig, B.H. Fernández, J.M. González-Granado, G. van Niel, A. Boissonnas, M. Piel, and N. Manel. 2022. Nuclear envelope disruption triggers hallmarks of aging in lung alveolar macrophages. *Biorxiv*. 2022.02.17.480837. doi:10.1101/2022.02.17.480837.

Siniossoglou, S. 2013. Phospholipid metabolism and nuclear function: roles of the lipin family of phosphatidic acid phosphatases. *Biochimica et biophysica acta*. 1831:575–581. doi:10.1016/j.bbalip.2012.09.014.

Siniossoglou, S., H. Santos-Rosa, J. Rappsilber, M. Mann, and E. Hurt. 1998. A novel complex of membrane proteins required for formation of a spherical nucleus. *Embo J*. 17:6449–6464. doi:10.1093/emboj/17.22.6449.

Srivastava, N., G.P. de F. Nader, A. Williart, R. Rollin, D. Cuvelier, A. Lomakin, and M. Piel. 2021. Nuclear fragility, blaming the blebs. *Curr Opin Cell Biol*. 70:100–108. doi:10.1016/j.ceb.2021.01.007.

Stephens, A.D., P.Z. Liu, E.J. Banigan, L.M. Almassalha, V. Backman, S.A. Adam, R.D. Goldman, and J.F. Marko. 2017. Chromatin histone modifications and rigidity affect nuclear morphology independent of lamins. *Molecular Biology of the Cell*. 29:mbc.E17-06-0410-233. doi:10.1091/mbc.e17-06-0410.

Takaki, T., M. Montagner, M.P. Serres, M.L. Berre, M. Russell, L. Collinson, K. Szuhai, M. Howell, S.J. Boulton, E. Sahai, and M. Petronczki. 2017. Actomyosin drives cancer cell nuclear dysmorphia and threatens genome stability. *Nature communications*. 8:16013. doi:10.1038/ncomms16013.

Tamiello, C., M.A.F. Kamps, A. van den Wijngaard, V.L.R.M. Verstraeten, F.P.T. Baaijens, J.L.V. Broers, and C.C.V. Bouten. 2013. Soft substrates normalize nuclear morphology and prevent nuclear rupture in fibroblasts from a laminopathy patient with compound heterozygous LMNA mutations. *Nucleus*. 4:61–73. doi:10.4161/nucl.23388.

Tanaka, S.S., A. Nakane, Y.L. Yamaguchi, T. Terabayashi, T. Abe, K. Nakao, M. Asashima, K.A. Steiner, P.P.L. Tam, and R. Nishinakamura. 2013. Dullard/Ctdnep1 Modulates WNT Signalling Activity for the Formation of Primordial Germ Cells in the Mouse Embryo. *Plos One*. 8:e57428. doi:10.1371/journal.pone.0057428.

Ungricht, R., and U. Kutay. 2017. Mechanisms and functions of nuclear envelope remodelling. *Nature Reviews Molecular Cell Biology*. 18:229–245. doi:10.1038/nrm.2016.153.

Vargas, J.D., E.M. Hatch, D.J. Anderson, and M.W. Hetzer. 2012. Transient nuclear envelope rupturing during interphase in human cancer cells. *Nucleus*. 3:88–100. doi:10.4161/nucl.18954.

Venturini, V., F. Pezzano, F.C. Castro, H.-M. Häkkinen, S. Jiménez-Delgado, M. Colomer-Rosell, M. Marro, Q. Tolosa-Ramon, S. Paz-López, M.A. Valverde, J. Weghuber, P. Loza-Alvarez, M. Krieg, S. Wieser, and V. Ruprecht. 2020. The nucleus measures shape changes for cellular proprioception to control dynamic cell behavior. *Science (New York, N.Y.)*. 370. doi:10.1126/science.aba2644.

Vietri, M., S.W. Schultz, A. Bellanger, C.M. Jones, L.I. Petersen, C. Raiborg, E. Skarpen, C.R.J. Pedurupillay, I. Kjos, E. Kip, R. Timmer, A. Jain, P. Collas, R.L. Knorr, S.N. Grellscheid, H. Kusumaatmaja, A. Brech, F.

Micci, H. Stenmark, and C. Campsteijn. 2020. Unrestrained ESCRT-III drives micronuclear catastrophe and chromosome fragmentation. *Nature cell biology*. 22:856–867. doi:10.1038/s41556-020-0537-5.

Vos, W.H.D., F. Houben, M. Kamps, A. Malhas, F. Verheyen, J. Cox, E.M.M. Manders, V.L.R.M. Verstraeten, M.A.M. van Steensel, C.L.M. Marcelis, A. van den Wijngaard, D.J. Vaux, F.C.S. Ramaekers, and J.L.V. Broers. 2011. Repetitive disruptions of the nuclear envelope invoke temporary loss of cellular compartmentalization in laminopathies. *Hum Mol Genet*. 20:4175–4186. doi:10.1093/hmg/ddr344.

Wang, S., H. Tukachinsky, F.B. Romano, and T.A. Rapoport. 2016. Cooperation of the ER-shaping proteins atlastin, lunapark, and reticulons to generate a tubular membrane network. *Elife*. 5:e18605. doi:10.7554/elife.18605.

Witkin, K.L., Y. Chong, S. Shao, M.T. Webster, S. Lahiri, A.D. Walters, B. Lee, J.L.Y. Koh, W.A. Prinz, B.J. Andrews, and O. Cohen-Fix. 2012. The Budding Yeast Nuclear Envelope Adjacent to the Nucleolus Serves as a Membrane Sink during Mitotic Delay. *Curr Biol*. 22:1128–1133. doi:10.1016/j.cub.2012.04.022.

Xia, Y., I.L. Ivanovska, K. Zhu, L. Smith, J. Irianto, C.R. Pfeifer, C.M. Alvey, J. Ji, D. Liu, S. Cho, R.R. Bennett, A.J. Liu, R.A. Greenberg, and D.E. Discher. 2018. Nuclear rupture at sites of high curvature compromises retention of DNA repair factors. *Journal of Cell Biology*. 217:3796–3808. doi:10.1083/jcb.201711161.

Xia, Y., C.R. Pfeifer, K. Zhu, J. Irianto, D. Liu, K. Pannell, E.J. Chen, L.J. Dooling, M.P. Tobin, M. Wang, I.L. Ivanovska, L.R. Smith, R.A. Greenberg, and D.E. Discher. 2019. Rescue of DNA damage after constricted migration reveals a mechano-regulated threshold for cell cycle. *Journal of Cell Biology*. 218:2545–2563. doi:10.1083/jcb.201811100.

Yang, Z., J. Maciejowski, and T. de Lange. 2017. Nuclear envelope rupture is enhanced by loss of p53 or Rb. *Molecular cancer research : MCR*. 15:molcanres.0084.2017-1586. doi:10.1158/1541-7786.mcr-17-0084.

Young, A.M., A.L. Gunn, and E.M. Hatch. 2020. BAF facilitates interphase nuclear membrane repair through recruitment of nuclear transmembrane proteins. *Mol Biol Cell*. 31:1551–1560. doi:10.1091/mbc.e20-01-0009.

Zhang, Q., A.C. Tamashunas, A. Agrawal, M. Torbati, A. Katiyar, R.B. Dickinson, J. Lammerding, and T.P. Lele. 2019. Local, transient tensile stress on the nuclear membrane causes membrane rupture. *Molecular Biology of the Cell*. 30:899–906. doi:10.1091/mbc.e18-09-0604.

Zhou, X., Y. He, X. Huang, Y. Guo, D. Li, and J. Hu. 2019. Reciprocal regulation between lunapark and atlastin facilitates ER three-way junction formation. *Protein Cell*. 10:510–525. doi:10.1007/s13238-018-0595-7.

Figure Legends

Figure 1. RFP-Cyto is size excluded from re-compartmentalization following nuclear rupture.
(A) Schematic of RFP-Cyto (top) and GFP-Nuc (bottom) reporters for nuclear rupture. **(B)** Schematic of cells with integrated RFP-Cyto and GFP-Nuc reporters before, during, and following nuclear rupture. **(C)** Mean nuclear intensity traces segmented from nucleus with Stardist-Trackmate (simple LAP tracker) for a cell with no event and a rupture. Shown are both individual timepoints (dots) and smoothed line with loess smoothing (span = 0.2) overlay. Dashed line = start of event, RFP-Cyto = magenta, GFP-Nuc = cyan **(D)** Representative image panel from a rupturing nucleus, traced in c. Scale bar = 10 microns, time stamp hh:mm **(E)** Precision and recall analysis. n = 297 cells, 25 rupturing nuclei (N1), n = 390 cells, 44 rupturing nuclei (N2), N = 2, false discovery rate = 0.014 **(F)** Rupture frequency of cells transfected with siRNA, as noted, fixed (dark blue) or live imaged 18-20 h (light blue). Individual points indicate separate experiments. Fixed: N = 4, n = 1471 (CTRL), 1177 (LMNA), 612 (LMNB1), 1193 (SUN1), live: N = 2, n = 187 (CTRL), 153 (LMNA), 112 (LMNB1), 165 (SUN1), * indicates p-value = 3.25e-03 (LMNA, fixed), 2.64e-03 (LMNB1, fixed), 5.90e-08 (SUN1, fixed), 1.28e-08 (LMNB1, live), 3.69e-02 (SUN1, live). All experiments completed in a stable U2OS shLMNB1 GFP-Nuc RFP-Cyto (U2OS RuptR) cell line.

Figure 2. Pipeline for automated fixed cell analysis using RFP-Cyto.
(A) Experimental design schematic. **(B)** Analysis pipeline design schematic indicating R filters applied globally (intensity filters) or by well (size/shape filters) and the approximate percentage of objects removed from validation wells prior to rupture determination **(C)** Representative image panel from CellProfiler. Outlines indicate pipeline stage in (B), channel indicated on top. Raw = original images (background subtracted and rescaled intensity), true segment = nuclear/cytoplasmic segment outlines produce by CellProfiler used for size/shape measurements, eroded segment: intensity measurement segmentation reduced for margin of error. **(D)** RFP channel (from (C)) overlaid with nuclear:cytoplasmic RFP-Cyto ratio values and nuclei false colored by passing filters, next to RFP/GFP merge image. Scale bar = 10 microns.

Figure 3. High content siRNA screen of fixed U2OS RuptR cells identifies changes to rupture frequency.
(A) Boxplot of selected results with individual nuclei overlay, showing distribution of nuc:cyto RFP n = 2192 (CTRL), 1262 (LMNA), 1248 (LMNB1), 1521 (SUN1), N = 4, p-values = 7.64e-07 (LMNA), 2.41e-06 (LMNB1), 2.79e-67 (SUN1) (Wilcoxon test) **(B)** Volcano plot, x = log2(fold change) nuc:cyto RFP, y = -log10(unadjusted p-value) (Barnards test), red = Bonferroni adjusted $p < 0.05$, red points labeled with siRNA. **(C)** Table of siRNAs with rupture frequency normalized to CTRL value. Bonferroni adjusted p-value (Barnards test) shown as p-value. **(D)** Bar plot of rupture frequency, normalized to CTRL, for single siRNA transfection of select hits from the screen. n = 2156 (ARID4A), 1411 (CTDNEP1), 1411 (CTRL), 1334 (MYCBP2), 2025 (NDC1), 1778 (NRM), 2141 (RASA1). N = 4, stats = Barnards test, adjusted for false discovery rate 0.07, p-values = 5.00e-08 (ARID4A), 5.55e-14 (CTDNEP1), 2.80e-02 (MYCBP2), 1.60e-04 (NDC1), 6.65e-18 (NRM), 2.60e-02 (RASA1). **(E)** Median nucleus area (pixels^2) and rupture frequency show no correlation. Pearson's correlation coefficient (r) = 0.13.

Figure 4. Screen hits enriched for cytoskeleton and nuclear membrane/ER regulators.
(A,B) Enrichment of gene sets associated with significant rupture frequency ($p <= 0.05$ Bonferroni adjusted p-value) within gene sets associated with the screen (Broad Institute, C5:GO Biological Pathways (A) and Cellular Component(B)). Size = enrichment p-value, color = screen rupture frequency, green = low, maroon = high.

Figure 5. CTDNEP1 depletion causes increased nuclear rupture frequency.
(A) Representative image panel of U2OS shLMNB1 cells transfected with siRNA as indicated, labeled with antibodies to calreticulin, and stained with DAPI. Cyan = DAPI, magenta = calreticulin. Scale bar = 10 microns **(B)** Rupture frequency of U2OS shLMNB1 and HeLa cells transfected with siCTRL or siCTDNEP1_9 as indicated, n = 113 (CTRL, N1), 104 (CTRL, N2), 165 (CTRL, N3), 123 (CTDNEP1, N1), 95 (CTDNEP1, N2), 127 (CTDNEP1, N3). * = p-value (Barnards test) 1.41e-11(U2OS), 5.69e-12 (HeLa) **(C)** Rupture duration in U2OS shLMNB1 cells transfected with siRNA as indicated. Boxplot = pooled population by experiment, points = individual ruptures. n(ruptures) = 180 (CTRL, N1), 115 (CTRL, N2), 105 (CTRL, N3), 156 (CTDNEP1, N1), 109 (CTDNEP1, N2), 120 (CTDNEP1, N3), total cells = 44 (CTRL, N1),32 (CTRL, N2), 30 (CTRL, N3), 18 (CTDNEP1, N1), 27 (CTDNEP1, N2),29 (CTDNEP1, N3).

Supplemental Figure Legends

Supplemental Figure 1.

(A) Rupture frequency and p-values (Barnards test) associated with Fig. 1F. **(B)** Representative nuclear:cytoplasmic RFP-Cyto traces (manually segmented) normalized to the starting frame, corrected for frame average intensities, for nuclei that remain intact (n = 5, left) and nuclei with at least one rupture (n = 5, right). Ruptured cells traced from just before the rupture, continuing through the end of imaging. Dashed line = baseline for comparison. **(C)** A mitotic cell was manually segmented and traced through mitosis, along with daughter cells. Shown is the nuc:cyto ratios for GFP and RFP, normalized to the beginning frame. Magenta = RFP-Cyto, Green = GFP-Nuc. Mitosis duration shown in blue, corresponds to Movie S2.

Supplemental Figure 2.

(A) Schematic of the CellProfiler segmentation pipeline. Nucleus and cytoplasm masks were generated from Hoechst and RFP, respectively, from which area and shape measurements were taken. These masks were eroded (right) prior to taking mean intensity fluorescent measurements of the Hoechst/RFP channels.

Supplemental Figure 3.

(A) Enrichment of gene sets available in the Broad Institute C5:GO Biological Pathways database within all genes included in the siRNA screen. p-values indicated on the right of plot and by heat map legend (**B)** Bar plot of rupture frequency results (y-axis) of siRNA screen. Gold = results of individual experiments, light blue = select genes with known results **(C)** Left: precision and recall, right: segmentation analysis of select wells, false discovery rate = 0.07, n = 22 (CTRL), 26 (LMNB1), 39 (CTDNEP1), 30 (TEN1), 12 (POMGNT2), 30 (LY9) , 29 rupturing nuclei, N = 3 **(D-E).** Selected results for low (green) and high (maroon) area (d) or solidity (e) based on screen results, n = 564 (POMGNT2), 1248 (LMNB1), 2192 (CTRL), 1209 (CTDNEP1), 1065 (TEN1), N 3-4 area p-values = 5.01e-23 (POMGNT2), 2.68e-20 (LMNB1), 8.79e-19 (CTDNEP1), 3.27e-43 (TEN1), solidity p-values = 1.70e-09 (CTDNEP1), 8.30e-28 (LY9) by Wilcoxon rank-sum test. **(F)** Representative images of nuclei indicated in (D-E). Scale bar = 10 microns. **(G)** Representative images of RFP, GFP, and Hoechst channels for CTRL and PSMC1 siRNA wells. Scale bar = 10 microns. All experiments completed in U2OS RuptR cells.

Supplemental Figure 4.

(A) Enrichment of gene sets associated with significant rupture frequency (p <= 0.05 adjusted p-value) within gene sets associated with the screen, genes categorized by whether they were specifically selected (Targeted) for inclusion or chosen by random number generator (Non-Targeted).

Supplemental Figure 5.

(A) Relative expression by qRT-PCR of CTDNEP1 in U2OS shLmnB1 or HeLa cells transfected with CTRL, CTDNEP1_9, or CTDNEP1_10 siRNAs. N = 3. **(B)** Rupture frequency in U2OS-shLMNB1 or HeLa cells transfected with CTRL or CTDNEP1-10 siRNAs, as indicated. n = 113 (CTRL, N1), 104 (CTRL, N2), 165

(CTRL, N3), 118 (CTDNEP1-10, N1), 104 CTDNEP1-10, N2), 152 (CTDNEP1-10, N3), p-value = 1.71e-12 (Barnards).

Supplemental Movie S1. Shown are a rupturing (right) and non-rupturing (left) U2OS RuptR cells, associated with Fig. 1C-D. Channel order = RFP-Cyto, GFP-Nuc, merge. Scale bar = 10 microns. Time stamp = hh:mm. Movie speed = 7 fps.

Supplemental Movie S2. Shown is a mitotic U2OS RuptR cell, associated with Fig. S3C, channel order RFP-Cyto, GFP-Nuc, merge. Scale bar = 10 microns, time stamp = hh:mm, image speed = 7 fps.

Supplemental Movie S3. Shown are nuclear ruptures in U2OS shLMNB1 RFP-NLS transfected with siCTRL and siCTDNEP1 siRNAs. Channel = RFP-NLS. Scale bar = 10 microns, time stamp = hh:mm, image speed = 7 fps.

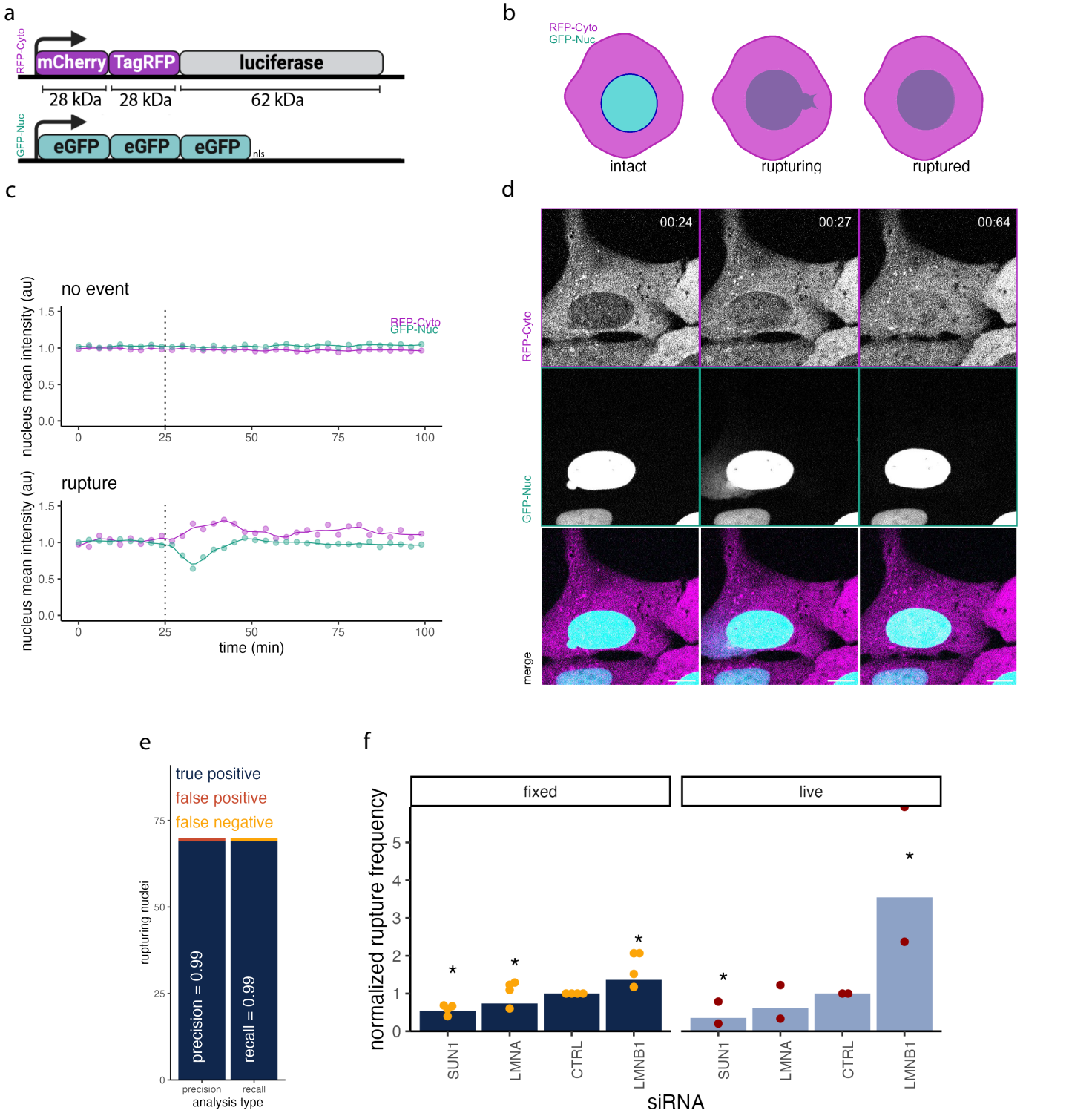

Figure 1. RFP-Cyto is size excluded from re-compartmentalization following nuclear rupture.
(A) Schematic of RFP-Cyto (top) and GFP-Nuc (bottom) reporters for nuclear rupture. (B) Schematic of cells with integrated RFP-Cyto and GFP-Nuc reporters before, during, and following nuclear rupture. (C) Mean nuclear intensity traces segmented from nucleus with Stardist-Trackmate (simple LAP tracker) for a cell with no event and a rupture. Shown are both individual timepoints (dots) and smoothed line with loess smoothing (span = 0.2) overlay. Dashed line = start of event, RFP-Cyto = magenta, GFP-Nuc = cyan (D) Representative image panel from a rupturing nucleus, traced in c. Scale bar = 10 microns, time stamp hh:mm (E) Precision and recall analysis. n = 297 cells, 25 rupturing nuclei (N1), n = 390 cells, 44 rupturing nuclei (N2), N = 2, false discovery rate = 0.014 (F) Rupture frequency of cells transfected with siRNA, as noted, fixed (dark blue) or live imaged 18-20 h (light blue). Individual points indicate separate experiments. Fixed: N = 4, n = 1471 (CTRL), 1177 (LMNA), 612 (LMNB1), 1193 (SUN1), live: N = 2, n = 187 (CTRL), 153 (LMNA), 112 (LMNB1), 165 (SUN1), * indicates p-value = 3.25e-03 (LMNA, fixed), 2.64e-03 (LMNB1, fixed), 5.90e-08 (SUN1, fixed), 1.28e-08 (LMNB1, live), 3.69e-02 (SUN1, live). All experiments completed in a stable U2OS shLMNB1 GFP-Nuc RFP-Cyto (U2OS RuptR) cell line.

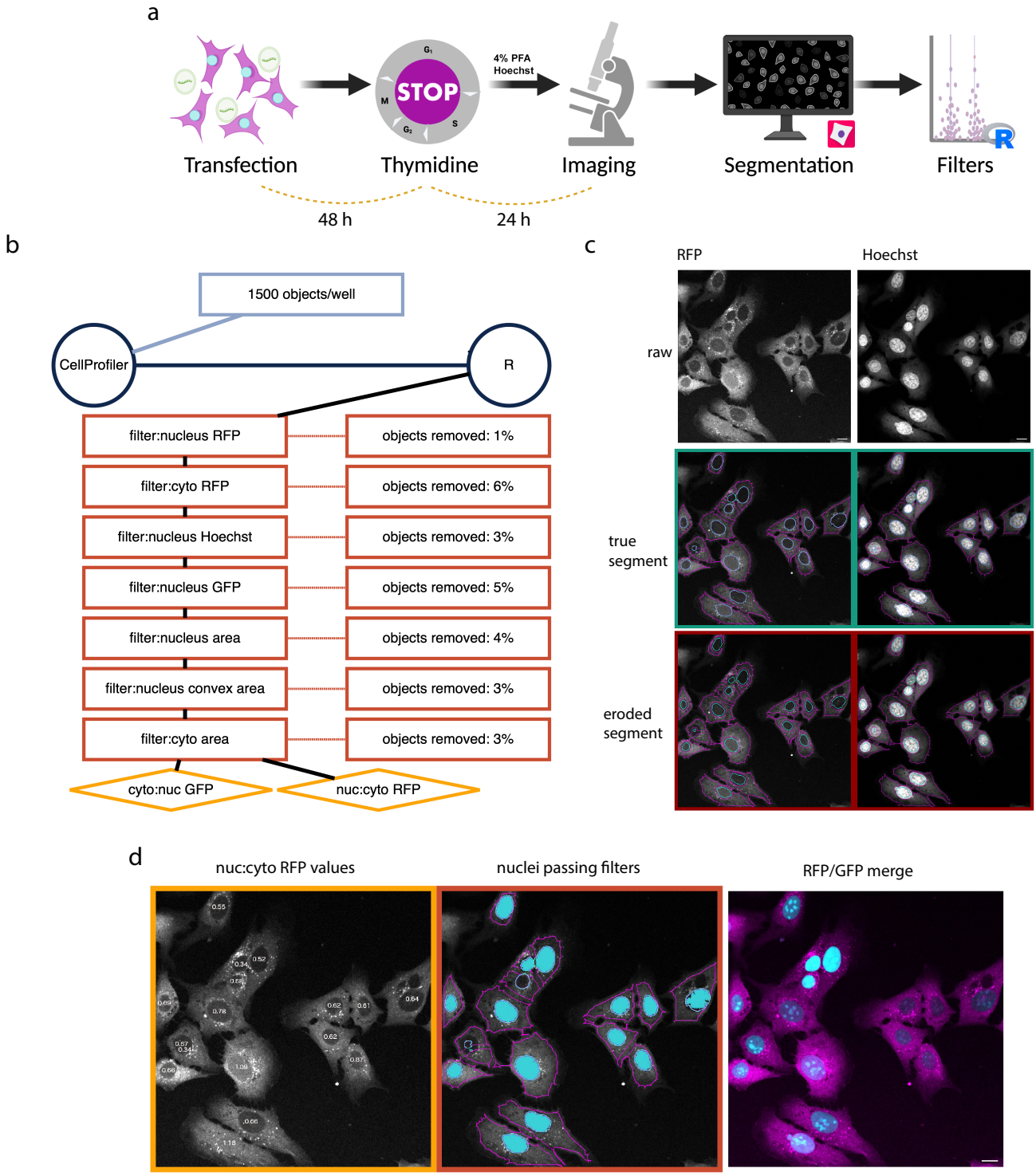

Figure 2. Pipeline for automated fixed cell analysis using RFP-Cyto.
(A) Experimental design schematic. (B) Analysis pipeline design schematic indicating R filters applied globally (intensity filters) or by well (size/shape filters) and the approximate percentage of objects removed from validation wells prior to rupture determination (C) Representative image panel from CellProfiler. Outlines indicate pipeline stage in (B), channel indicated on top. Raw = original images (background subtracted and rescaled intensity), true segment = nuclear/cytoplasmic segment outlines produce by CellProfiler used for size/shape measurements, eroded segment: intensity measurement segmentation reduced for margin of error. (D) RFP channel (from (C)) overlaid with nuclear:cytoplasmic RFP-Cyto ratio values and nuclei false colored by passing filters, next to RFP/GFP merge image. Scale bar = 10 microns.

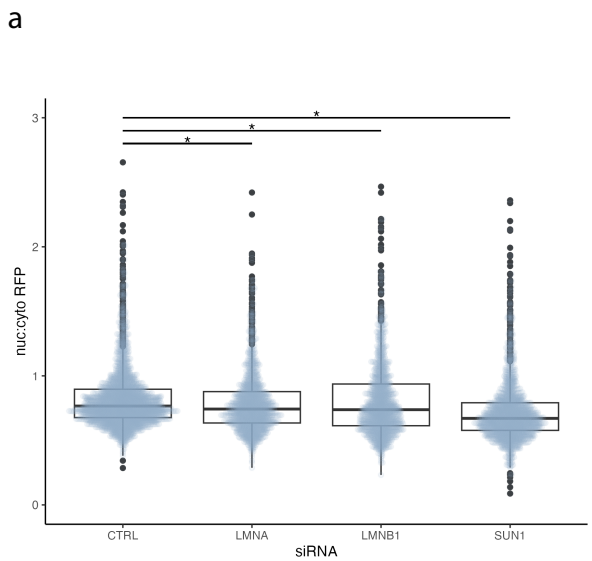

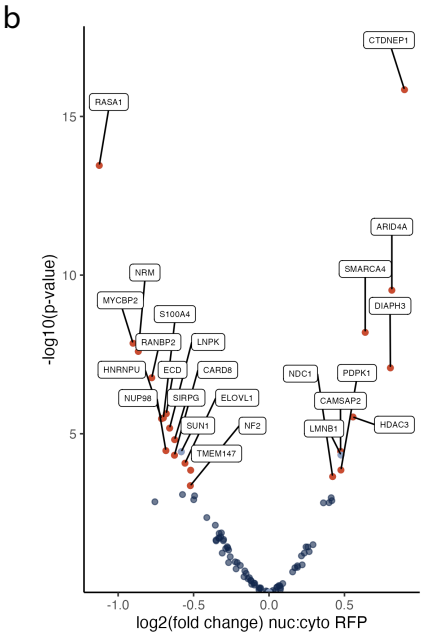

c

siRNA	function	normalized rupture frequency	p-value
ARID4A	transcription	1.7580004	2.82e-08
CAMSAP2	cytoskeleton	1.3893184	3.37e-03
CARD8	signaling, immune	0.6476327	4.47e-03
CTDNEP1	membrane structure	1.8632574	1.35e-14
DIAPH3	cytoskeleton	1.7464943	7.89e-06
ECD	transcription	0.6237480	2.19e-04
ELOVL1	membrane structure	0.6796947	7.96e-03
HDAC3	transcription	1.4705852	2.79e-04
HNRNPU	chromatin structure	0.6102693	3.16e-04
LNPK	membrane structure	0.6333841	6.26e-04
MYCBP2	unknown	0.5353296	1.32e-06
NDC1	npc	1.3394277	2.11e-02
NF2	signaling, proliferation	0.6966223	4.07e-02
NRM	net	0.5484291	2.39e-06
NUP98	npc	0.6226308	3.20e-03
PDPK1	signaling, proliferation	1.3912901	1.31e-02
RANBP2	npc	0.5834442	1.62e-05
RASA1	signaling, proliferation	0.4584430	3.29e-12
S100A4	cytoskeleton	0.6154313	2.99e-04
SIRPG	signaling	0.6481820	1.44e-03
SMARCA4	transcription	1.5555684	6.00e-07
TMEM147	translation	0.6976673	1.33e-02

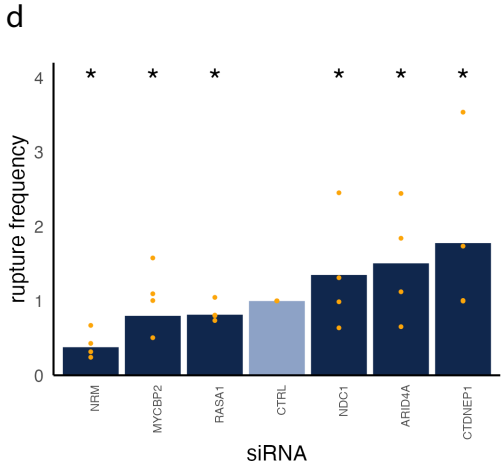

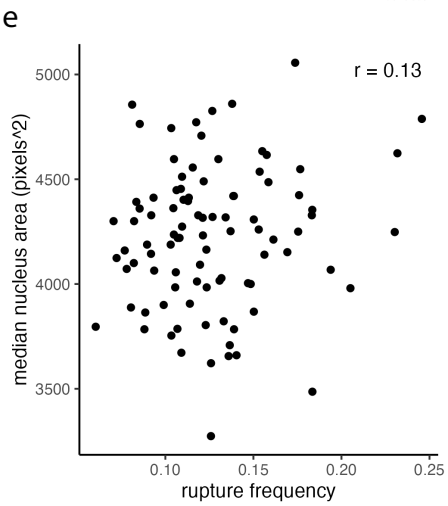

Figure 3. High content siRNA screen of fixed U2OS RuptR cells identifies changes to rupture frequency.
(A) Boxplot of selected results with individual nuclei overlay, showing distribution of nuc:cyto RFP n = 2192 (CTRL), 1262 (LMNA), 1248 (LMNB1), 1521 (SUN1), N = 4, p-values = 7.64e-07 (LMNA), 2.41e-06 (LMNB1), 2.79e-67 (SUN1) (Wilcoxon test) (B) Volcano plot, x = log2(fold change) nuc:cyto RFP, y = -log10(unadjusted p-value) (Barnards test), red = Bonferroni adjusted $p < 0.05$, red points labeled with siRNA. (C) Table of siRNAs with rupture frequency normalized to CTRL value. Bonferroni adjusted p-value (Barnards test) shown as p-value. (D) Bar plot of rupture frequency, normalized to CTRL, for single siRNA transfection of select hits from the screen. n = 2156 (ARID4A), 1411 (CTDNEP1), 1411 (CTRL), 1334 (MYCBP2), 2025 (NDC1), 1778 (NRM), 2141 (RASA1). N = 4, stats = Barnards test, adjusted for false discovery rate 0.07, p-values = 5.00e-08 (ARID4A), 5.55e-14 (CTDNEP1), 2.80e-02 (MYCBP2), 1.60e-04 (NDC1), 6.65e-18 (NRM), 2.60e-02 (RASA1). (E) Median nucleus area (pixels2) and rupture frequency show no correlation. Pearson's correlation coefficient (r) = 0.13.

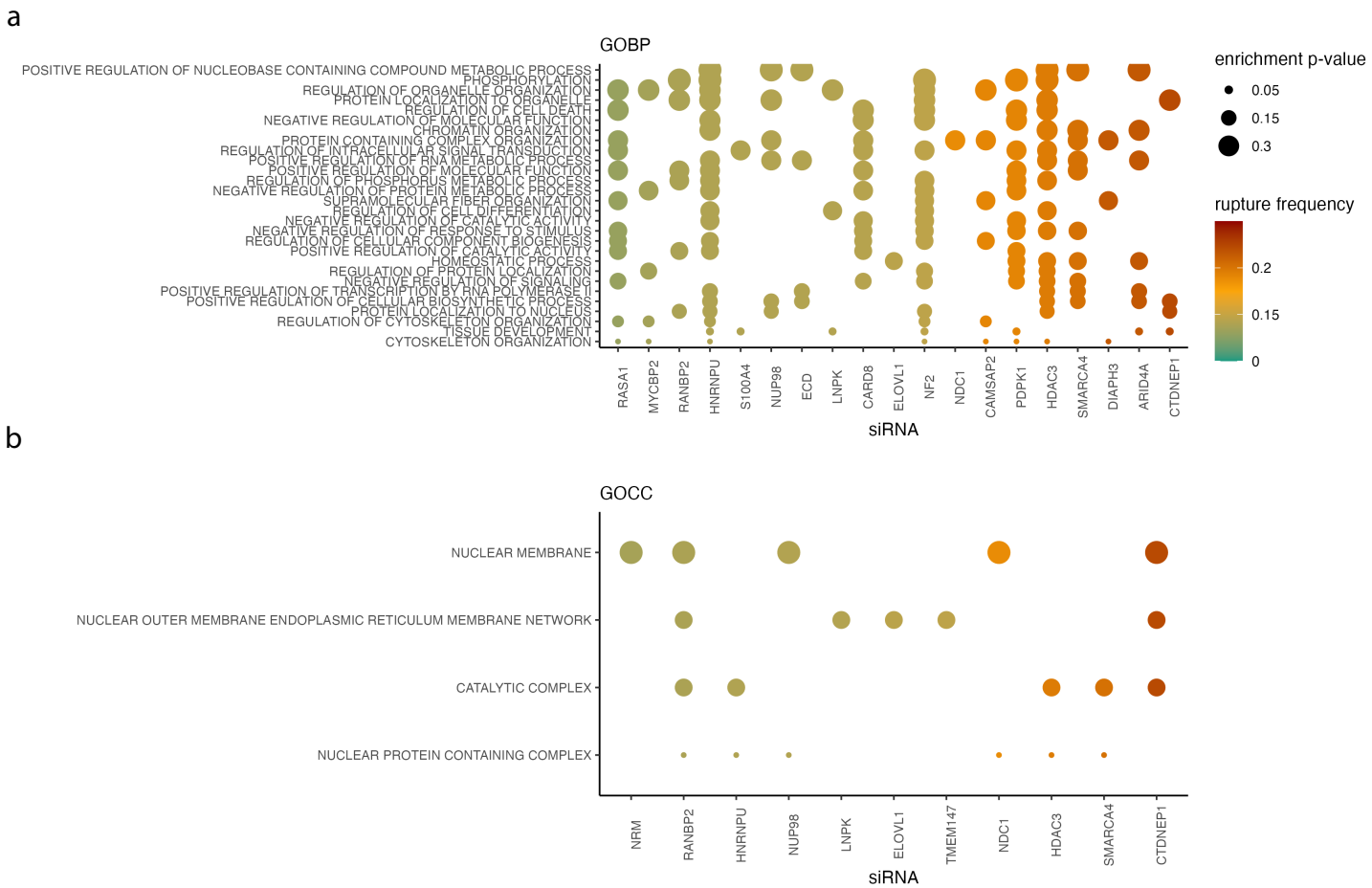

Figure 4. Screen hits enriched for cytoskeleton and nuclear membrane/ER regulators.
(A,B) Enrichment of gene sets associated with significant rupture frequency ($p <= 0.05$ Bonferroni adjusted p-value) within gene sets associated with the screen (Broad Institute, C5:GO Biological Pathways (A) and Cellular Component(B)). Size = enrichment p-value, color = screen rupture frequency, green = low, maroon = high.

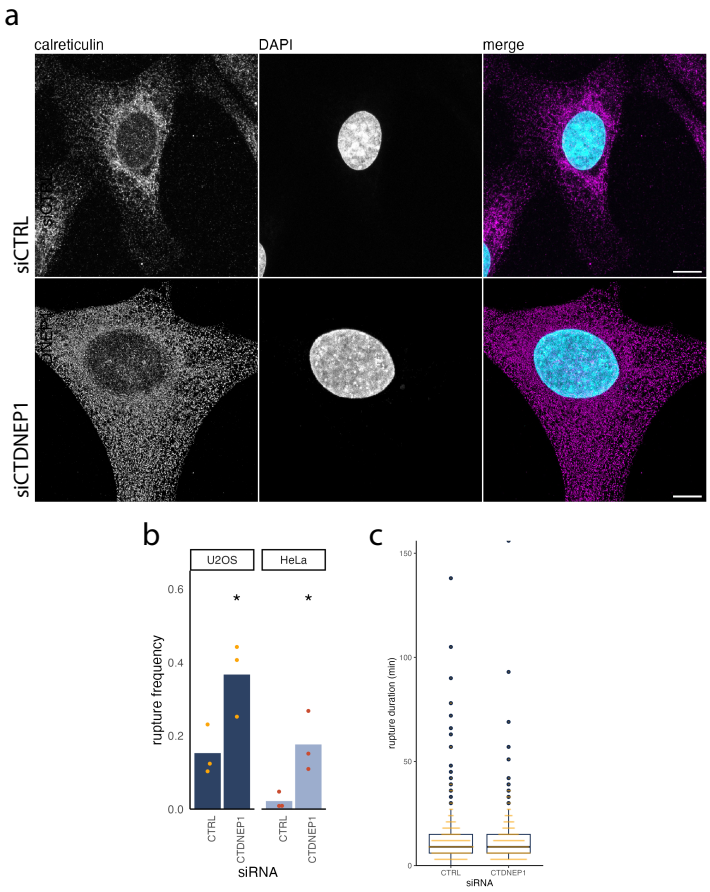

Figure 5. CTDNEP1 depletion causes increased nuclear rupture frequency.
(A) Representative image panel of U2OS shLMNB1 cells transfected with siRNA as indicated, labeled with antibodies to calreticulin, and stained with DAPI. Cyan = DAPI, magenta = calreticulin. Scale bar = 10 microns (B) Rupture frequency of U2OS shLMNB1 and HeLa cells transfected with siCTRL or siCTDNEP1_9 as indicated, n = 113 (CTRL, N1), 104 (CTRL, N2), 165 (CTRL, N3), 123 (CTDNEP1, N1), 95 (CTDNEP1, N2), 127 (CTDNEP1, N3). * = p-value (Barnards test) 1.41e-11(U2OS), 5.69e-12 (HeLa) (C) Rupture duration in U2OS shLMNB1 cells transfected with siRNA as indicated. Boxplot = pooled population by experiment, points = individual ruptures. n(ruptures) = 180 (CTRL, N1), 115 (CTRL, N2), 105 (CTRL, N3), 156 (CTDNEP1, N1), 109 (CTDNEP1, N2), 120 (CTDNEP1, N3), total cells = 44 (CTRL, N1),32 (CTRL, N2), 30 (CTRL, N3), 18 (CTDNEP1, N1), 27 (CTDNEP1, N2),29 (CTDNEP1, N3).

a

siRNA	type	rupture frequency	p-value
CTRL	live	0.0855615	1.00e+00
LMNA	live	0.0522876	1.11e-01
LMNB1	live	0.3035714	1.28e-08
SUN1	live	0.0303030	3.69e-02
CTRL	fixed	0.1475187	1.00e+00
LMNA	fixed	0.1087511	3.25e-03
LMNB1	fixed	0.2009804	2.65e-03
SUN1	fixed	0.0796312	5.90e-08

b

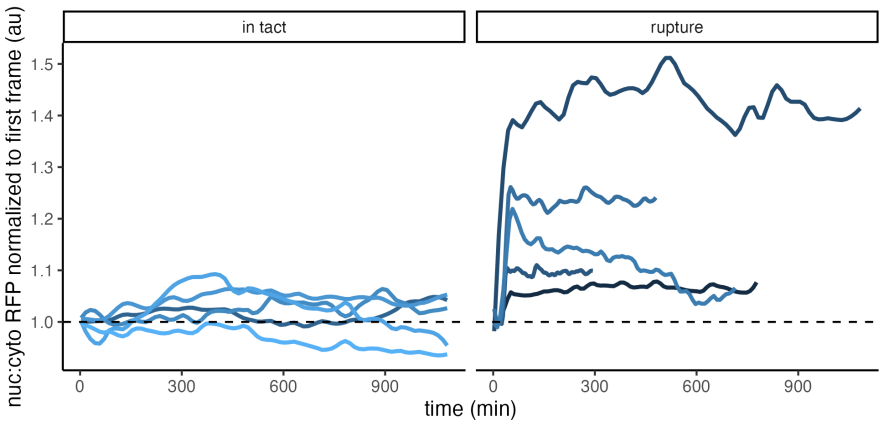

c

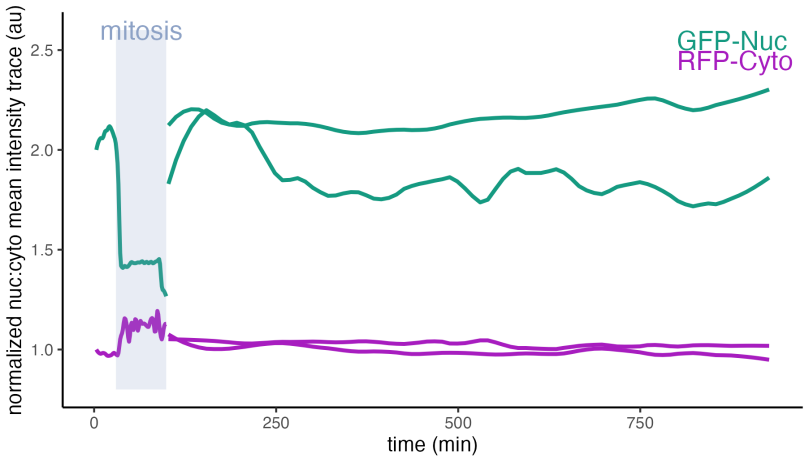

Supplemental Figure 1.
(A) Rupture frequency and p-values (Barnards test) associated with Fig. 1F. (B) Representative nuclear:cytoplasmic RFP-Cyto traces (manually segmented) normalized to the starting frame, corrected for frame average intensities, for nuclei that remain intact (n = 5, left) and nuclei with at least one rupture (n = 5, right). Ruptured cells traced from just before the rupture, continuing through the end of imaging. Dashed line = baseline for comparison. (C) A mitotic cell was manually segmented and traced through mitosis, along with daughter cells. Shown is the nuc:cyto ratios for GFP and RFP, normalized to the beginning frame. Magenta = RFP-Cyto, Green = GFP-Nuc. Mitosis duration shown in blue, corresponds to Movie S2.

a

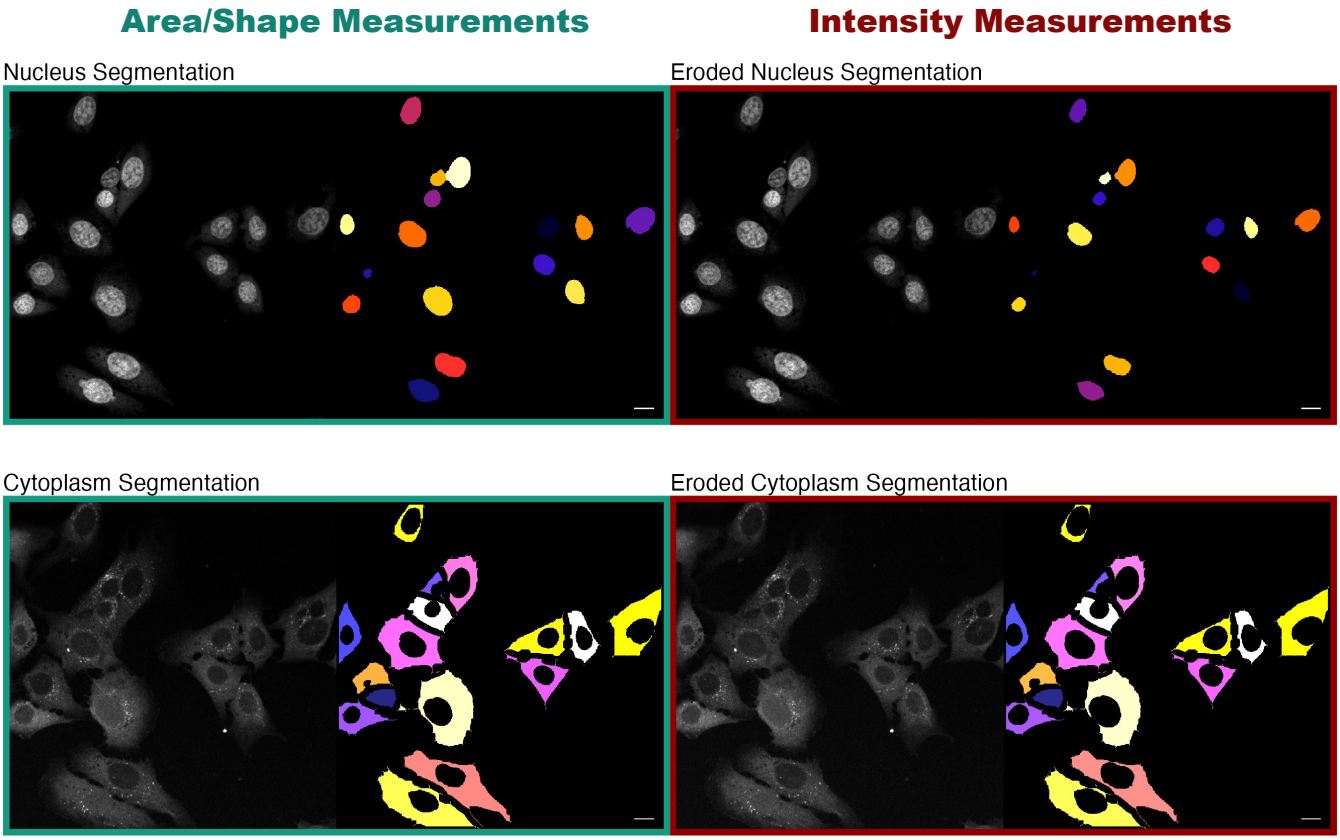

Supplemental Figure 2.
(A) Schematic of the CellProfiler segmentation pipeline. Nucleus and cytoplasm masks were generated from Hoechst and RFP, respectively, from which area and shape measurements were taken. These masks were eroded (right) prior to taking mean intensity fluorescent measurements of the Hoechst/RFP channels.

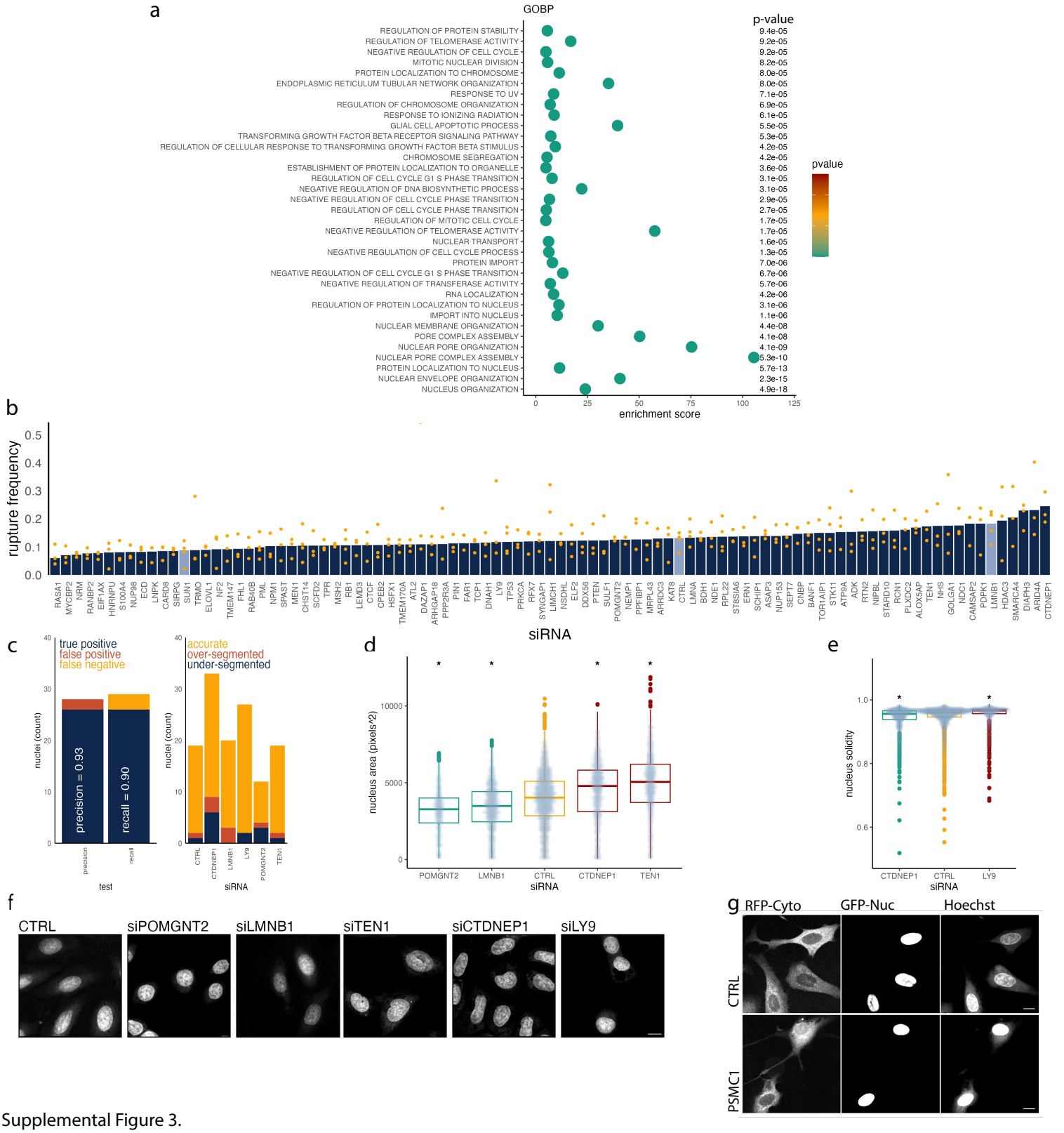

Supplemental Figure 3.

(A) Enrichment of gene sets available in the Broad Institute C5:GO Biological Pathways database within all genes included in the siRNA screen. p-values indicated on the right of plot and by heat map legend (B) Bar plot of rupture frequency results (y-axis) of siRNA screen. Gold = results of individual experiments, light blue = select genes with known results (C) Left: precision and recall, right: segmentation analysis of select wells, false discovery rate = 0.07, n = 22 (CTRL), 26 (LMNB1), 39 (CTDNEP1), 30 (TEN1), 12 (POMGNT2), 30 (LY9) , 29 rupturing nuclei, N = 3 (D-E). Selected results for low (green) and high (maroon) area (d) or solidity (e) based on screen results, n = 564 (POMGNT2), 1248 (LMNB1), 2192 (CTRL), 1209 (CTDNEP1), 1065 (TEN1), N 3-4 area p-values = 5.01e-23 (POMGNT2), 2.68e-20 (LMNB1), 8.79e-19 (CTDNEP1), 3.27e-43 (TEN1), solidity p-values = 1.70e-09 (CTDNEP1), 8.30e-28 (LY9) by Wilcoxon rank-sum test. (F) Representative images of nuclei indicated in (D-E). Scale bar = 10 microns. (G) Representative images of RFP, GFP, and Hoechst channels for CTRL and PSMC1 siRNA wells. Scale bar = 10 microns. All experiments completed in U2OS RuptR cells.

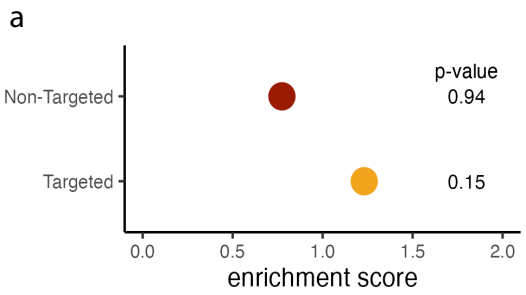

Supplemental Figure 4.
(A) Enrichment of gene sets associated with significant rupture frequency (p <= 0.05 adjusted p-value) within gene sets associated with the screen, genes categorized by whether they were specifically selected (Targeted) for inclusion or chosen by random number generator (Non-Targeted).

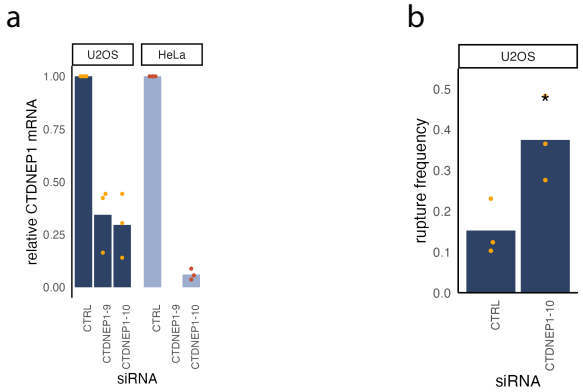

Supplemental Figure 5.
(A) Relative expression by qRT-PCR of CTDNEP1 in U2OS shLmnB1 or HeLa cells transfected with CTRL, CTDNEP1_9, or CTDNEP1_10 siRNAs. N = 3. (B) Rupture frequency in U2OS-shLMNB1 or HeLa cells transfected with CTRL or CTDNEP1-10 siRNAs, as indicated. n = 113 (CTRL, N1), 104 (CTRL, N2), 165 (CTRL, N3), 118 (CTDNEP1-10, N1), 104 CTDNEP1-10, N2), 152 (CTDNEP1-10, N3), p-value = 1.71e-12 (Barnards).